Eccentric binary black-hole mergers: The transition from inspiral to plunge in general relativity

Ulrich Sperhake,[1,*] Emanuele Berti,[2,3] Vitor Cardoso,[4,5] José A. González,[1,6] Bernd Brügmann,[1] and Marcus Ansorg[7]

[1]*Theoretisch Physikalisches Institut, Friedrich Schiller Universität, 07743 Jena, Germany*
[2]*Jet Propulsion Laboratory, California Institute of Technology, Pasadena, California 91109, USA*
[3]*McDonnell Center for the Space Sciences, Department of Physics, Washington University, St. Louis, MR 63130, USA*
[4]*Department of Physics and Astronomy, The University of Mississippi, University, Mississippi 38677-1848, USA*
[5]*Centro Multidisciplinar de Astrofísica–CENTRA, Departamento de Física, Instituto Superior Técnico, Avenida Rovisco Pais 1, 1049-001 Lisboa, Portugal*
[6]*Instituto de Física y Matemáticas, Universidad Michoacana de San Nicolás de Hidalgo, Edificio C-3, Ciudad Universitaria C. P. 58040 Morelia, Michoacán, México*
[7]*Max-Planck-Institut für Gravitationsphysik, Albert-Einstein-Institut, 14476 Golm, Germany*

(Received 22 October 2007; revised manuscript received 16 July 2008; published 29 September 2008)

We study the transition from inspiral to plunge in general relativity by computing gravitational waveforms of nonspinning, equal-mass black-hole binaries. We consider three sequences of simulations, starting with a quasicircular inspiral completing 1.5, 2.3 and 9.6 orbits, respectively, prior to coalescence of the holes. For each sequence, the binding energy of the system is kept constant and the orbital angular momentum is progressively reduced, producing orbits of increasing eccentricity and eventually a head-on collision. We analyze in detail the radiation of energy and angular momentum in gravitational waves, the contribution of different multipolar components and the final spin of the remnant, comparing numerical predictions with the post-Newtonian approximation and with extrapolations of point-particle results. We find that the motion transitions from inspiral to plunge when the orbital angular momentum $L = L_{\rm crit} \simeq 0.8M^2$. For $L < L_{\rm crit}$ the radiated energy drops very rapidly. Orbits with $L \simeq L_{\rm crit}$ produce our largest dimensionless Kerr parameter for the remnant, $j = J/M^2 \simeq 0.724 \pm 0.13$ (to be compared with the Kerr parameter $j \simeq 0.69$ resulting from quasicircular inspirals). This value is in good agreement with the value of 0.72 reported in [I. Hinder, B. Vaishnav, F. Herrmann, D. Shoemaker, and P. Laguna, Phys. Rev. D **77**, 081502 (2008).]. These conclusions are quite insensitive to the initial separation of the holes, and they can be understood by extrapolating point-particle results. Generalizing a model recently proposed by Buonanno, Kidder and Lehner [A. Buonanno, L. E. Kidder, and L. Lehner, Phys. Rev. D **77**, 026004 (2008).] to eccentric binaries, we conjecture that (1) $j \simeq 0.724$ is close to the maximal Kerr parameter that can be obtained by any merger of nonspinning holes, and (2) no binary merger (even if the binary members are extremal Kerr black holes with spins aligned to the orbital angular momentum, and the inspiral is highly eccentric) can violate the cosmic censorship conjecture.

DOI: 10.1103/PhysRevD.78.064069 PACS numbers: 04.25.dg, 04.25.Nx, 04.30.Db, 04.70.Bw

I. INTRODUCTION

The research area of gravitational wave (GW) physics has reached a very exciting stage, both experimentally and theoretically. Earth-based laser-interferometric detectors, including LIGO [1], GEO600 [2] and TAMA [3], are collecting data at design sensitivity, searching for GWs in the frequency range ~ 10–10^3 Hz. VIRGO [4] should reach design sensitivity within 1 yr, and the space-based interferometer LISA is expected to open an observational window at low frequencies ($\sim 10^{-4}$–10^{-1} Hz) within the next decade [5].

The last two years have also seen a remarkable breakthrough in the simulation of the strongest expected GW sources, the inspiral and coalescence of black-hole binaries [6–8]. Several groups have now generated independent numerical codes for such simulations [9–17] and studied various aspects of binary black-hole mergers. In the context of analyzing the resulting gravitational waveforms, these include, in particular, the comparisons of numerical results with post-Newtonian (PN) predictions [18–23], multipolar analyses of the emitted radiation [21,22,24], the use of numerical waveforms in data analysis [25–28] and gravitational wave emission from systems of three black holes [29].

Despite this progress, a comprehensive analysis of binary black-hole inspirals remains a daunting task, mainly because of the large dimensionality of the parameter space. In geometrical units, the total mass of the binary is just an overall scale factor. The source parameters to be explored by numerical simulations (sometimes called ''intrinsic'' parameters in the GW data analysis literature) include the mass ratio $q = M_2/M_1$, the eccentricity e of the orbit and six parameters for the magnitude of the individual black-hole spins and their direction with respect to the binary's orbital angular momentum.

In this paper we present results from numerical simulations of nonspinning, equal-mass black-hole binaries, and

*ulrich.sperhake@uni-jena.de

we focus on the effect of the orbital eccentricity on the merger waveforms. We consider three sequences, starting with quasicircular inspirals that complete ~ 1.5, ~ 2.3 and ~ 9.6 orbits, respectively, prior to coalescence of the holes. By fixing the binding energy of the system and progressively reducing the orbital angular momentum, we produce a sequence of orbits of increasing eccentricity and eventually a head-on collision. For each of these simulations we analyze in detail the radiation of energy and angular momentum in GWs, the contribution of different multipolar components and the final spin of the remnant, comparing numerical predictions with the PN approximation and with extrapolations of point-particle results.

Noneccentric inspirals are usually considered the most interesting cases for GW detection. For an isolated binary evolving under the effect of gravitational radiation reaction, the eccentricity decreases by roughly a factor of 3 when the orbital semimajor axis is halved [30]. For most conceivable formation mechanisms of solar-mass black-hole binaries, the orbit will usually be circular by the time the GW signal enters the best-sensitivity bandwidth of Earth-based interferometers. However, we wish to stress that our simulations could be of interest for GW detection. For example, according to some astrophysical scenarios, eccentric binaries may be potential GW sources for Earth-based detectors. In globular clusters, the inner binaries of hierarchical triplets undergoing Kozai oscillations can merge under gravitational radiation reaction, and $\sim 30\%$ of these systems can have eccentricity ~ 0.1 when GWs enter the detectors' most sensitive bandwidth at ~ 10 Hz [31]. Massive black-hole binaries to be observed by LISA could also have significant eccentricity in the last year of inspiral. Recent simulations using smoothed particle hydrodynamics follow the dynamics of binary black holes in massive, rotationally supported circumnuclear discs [32–34]. In these simulations, a primary black hole is placed at the center of the disc and a secondary black hole is set initially on an eccentric orbit in the disc plane. By using the particle splitting technique, the most recent simulations follow the binary's orbital decay down to distances ~ 0.1 pc. Dynamical friction is found to circularize the orbit if the binary *corotates* with the disc [33]. However, if the orbit is *counterrotating* with the disc the initial eccentricity does not seem to decrease, and black holes may still enter the GW emission phase with high eccentricity [32].

Complementary studies show that eccentricity evolution may still occur in later stages of the binary's life, because of close encounters with single stars and/or gas-dynamical processes. Three-body encounters with background stars have been studied mainly in spherical backgrounds. These studies find that stellar dynamical hardening can lead to an increase of the eccentricity, acting against the circularization driven by the large-scale action of the gaseous and/or stellar disc, possibly leaving the binary with nonzero eccentricity when gravitational radiation reaction becomes dominant [35–39]. It has also been suggested that the gravitational interaction of a binary with a circumbinary gas disc could increase the binary's eccentricity. The transition between disc-driven and GW-driven inspiral can occur at small enough radii that a small but significant eccentricity survives, typical values being $e \sim 0.02$ (with a lower limit $e \simeq 0.01$) 1 yr prior to merger (cf. Fig. 5 of [40]). If the binary has an "extreme" mass ratio $q \lesssim 0.02$ the residual eccentricity predicted by this scenario can be considerably larger, $e \gtrsim 0.1$. Numerical simulations should be able to test these predictions in the near future. As shown by Sopuerta, Yunes and Laguna, eccentricity could significantly increase the recoil velocity resulting from the merger of nonspinning black-hole binaries [41].

Independently of the presence of eccentricity in astrophysical binary mergers, the problem we consider here has considerable theoretical interest. Our simulations explore the transition between gravitational radiation from a quasicircular inspiral (the expected final outcome in most astrophysical scenarios) and the radiation emitted by a head-on collision, where the binary has maximal symmetry. Our work should provide some guidance for analytical studies of the "transition from inspiral to plunge." The first analytical study of this problem in the context of PN theory was carried out by Kidder, Will and Wiseman [42]. The transition between the adiabatic phase and the plunge was studied in [43] using nonperturbative resummed estimates of the damping and conservative parts of the two-body dynamics, i.e. the so-called "effective one body" (EOB) model. Ori and Thorne [44] provided a semianalytical treatment of the transition in the extreme mass-ratio limit. Waveforms comprising inspiral, merger and ringdown for comparable-mass bodies have also been produced using the EOB model (see e.g. [45] for extensions of the original model to spinning binaries and for references to previous work). Preliminary comparisons of EOB and numerical relativity waveforms showed that improved models of ringdown excitation [21,26,46] or additional phenomenological terms in the EOB effective potential [47] are needed to achieve acceptable phase differences between the numerical and analytical waveforms.

Our study is complementary to Ref. [48], which considered sequences of eccentric, equal-mass, nonspinning binary black-hole evolutions around the "threshold of immediate merger": a region of parameter space separating binaries that quickly merge to form a final Kerr black hole from those that do not merge in a short time. Similar scenarios have also been studied in Ref. [49], with particular regard to the maximal spin of the final hole generated in this way. The universality of the gravitational wave signal during the merger was analyzed in Ref. [50], where it was pointed out that binaries largely circularize after about 9 orbits when starting with eccentricities below about 0.4. The first comparison between numerical evolutions of

eccentric binaries with post-Newtonian predictions was presented in [51].

Our focus in this work is on the high-eccentricity region of the parameter space, which always leads to merger. In particular, the near-head-on limit of our study is of interest as a first step to compute the energy loss and production cross section of mini-black holes in TeV-scale gravity scenarios (possibly at the upcoming LHC [52]), and trans-Planckian scattering in general [53,54]. Present semi-analytical techniques (including a trapped surface search in the union of Aichelburg-Sexl shock waves, close-limit approximation calculations and perturbation theory) only give rough estimates of the emitted energy and production cross section [55] and do not provide much insight into the details of the process (but see [56] for a first numerical investigation).

Our main finding is that, for all sequences we studied, the motion radically changes character when the black holes' orbital angular momentum $L \sim L_{\rm crit} \simeq 0.8M^2$, turning from an eccentric inspiral into a plunge. In particular, for $L \lesssim L_{\rm crit}$ we observe that:

(i) The number of orbits $N_{\rm waves}$ (as estimated using the gravitational wave cycles) or $N_{\rm punc}$ (as computed from the punctures' trajectories) becomes less than 1, so the motion effectively turns into a plunge (see Table I and Fig. 4 below);

TABLE I. Sequences of models studied in this work. The irreducible mass of the individual black holes is $M_1 = M_2 = 0.5$ in all simulations, and consequently $\mu = 1/4$. The binding energy for sequence 1 (top 16 models in the table) is $E_{\rm b}^{(1)}/M = -0.014\,465$, that for sequence 2 (following 8 models) is $E_{\rm b}^{(2)}/M = -0.013\,229$ and that for sequence 3 (following 9 models) is $E_{\rm b}^{(3)} = -0.008\,861$. The bottom line lists parameters for a model which serves for estimating the uncertainties of the long simulations of sequence 3 (see Sec. III B) and has merely been included for completeness. $\Delta t_{\rm CAH}$ is the time of formation of a common apparent horizon as measured from the radiation peak, shifted by the extraction radius: $\Delta t_{\rm CAH} = t_{\rm CAH} + r_{\rm ex} - t_{\rm peak}$. For sequence 3, we have not calculated apparent horizons, and we estimate this quantity to be $\Delta t_{\rm CAH} = -16 M_{\rm ADM}$. $N_{\rm waves}$ and $N_{\rm punc}$ are the number of orbits obtained from the phase of the ($\ell = 2$, $m = 2$) multipole and the puncture's orbital motion, respectively. The last four columns list various PN estimates of the eccentricity (see Sec. II for a discussion).

$\frac{P}{M}$	$\frac{D}{M}$	$\frac{L}{M^2}$	$m_{1,2}$	$\frac{10^2 E_{\rm rad}}{M_{\rm ADM}}$	$\frac{J_{\rm rad}}{M_{\rm ADM}^2}$	$\frac{J_{\rm fin}}{M_{\rm fin}^2}$	$\frac{\Delta t_{\rm CAH}}{M_{\rm ADM}}$	$N_{\rm waves}$	$N_{\rm punc}$	e_t(ADMTT)	e_t(harm)	$e_{\rm MW}(M\Omega)$	$e_{\rm MW,circ}$
0.14	6.054	0.8476	0.4772	3.437	0.2257	0.6915	−15.95	1.32	1.51	0.0983	0.0987	0.1496 (0.0388)	0.0198
0.1383	6.131	0.8479	0.4775	3.451	0.2267	0.6910	−15.52	1.32	1.52	0.0956	0.0961	0.1458 (0.0391)	0.0188
0.13	6.528	0.8486	0.4790	3.478	0.2272	0.6916	−15	1.33	1.53	0.0878	0.0886	0.1353 (0.0398)	0.0162
0.12	7.064	0.8477	0.4808	3.494	0.2249	0.6932	−14.87	1.27	1.47	0.0977	0.0982	0.1488 (0.0389)	0.0196
0.11	7.672	0.8439	0.4825	3.530	0.2196	0.6953	−15.74	1.16	1.37	0.1306	0.1300	0.1948 (0.0359)	0.0336
0.10	8.361	0.8361	0.4842	3.486	0.2072	0.6994	−15.29	0.99	1.21	0.1800	0.1783	0.2674 (0.0319)	0.0634
0.09	9.140	0.8226	0.4857	3.261	0.1857	0.7043	−14.65	0.82	1.04	0.2424	0.2393	···	0.1194
0.08	10.013	0.8010	0.4872	2.839	0.1570	0.7051	−15.30	0.68	0.88	0.3161	0.3112	···	0.2370
0.07	10.978	0.7685	0.4885	2.259	0.1240	0.6964	−16.59	0.56	0.72	0.3995	0.3921	···	···
0.06	12.024	0.7215	0.4898	1.631	0.0909	0.6718	−16.53	0.43	0.59	0.4913	0.4799	···	···
0.05	13.121	0.6561	0.4908	1.061	0.0613	0.6257	−17.01	0.37	0.47	0.5887	0.5699	···	···
0.04	14.217	0.5687	0.4917	0.621	0.0379	0.5530	−17.67	0.31	0.36	0.6894	0.6540	···	···
0.03	15.234	0.4570	0.4924	0.328	0.0213	0.4510	−18.24	0.28	0.27	0.8050	0.7202	···	···
0.02	16.073	0.3214	0.4930	0.161	0.0106	0.3206	−19.11	0.24	0.17	1.1005	0.8090	···	···
0.01	16.630	0.1663	0.4933	0.080	0.0042	0.1669	−20.02	0.18	0.09	3.8101	2.5892	···	···
0	16.826	0	0.4934	0.057	0	0	−19.80	···	···	∞	∞	···	···
0.1247	7.000	0.8729	0.4798	3.585	0.2540	0.6912	−12.74	2.06	2.30	0.1095	0.1096	0.1529 (0.0323)	0.0202
0.12	7.278	0.8734	0.4807	3.581	0.2558	0.6897	−15.19	2.05	2.24	0.1049	0.1052	0.1468 (0.0326)	0.0186
0.10	8.678	0.8678	0.4841	3.659	0.2532	0.6875	−15.15	1.79	1.99	0.1480	0.1472	0.2049 (0.0295)	0.0363
0.08	10.493	0.8394	0.4871	3.602	0.2066	0.7053	−16	1.00	1.20	0.2758	0.2725	···	0.1320
0.06	12.754	0.7653	0.4897	2.181	0.1186	0.6974	−16.14	0.56	0.74	0.4567	0.4485	···	···
0.04	15.288	0.6115	0.4917	0.795	0.0471	0.5902	−17	0.27	0.46	0.6681	0.6428	···	···
0.02	17.488	0.3498	0.4930	0.185	0.0122	0.3378	−18.87	0.27	0.44	1.0122	0.8078	···	···
0	18.398	0	0.4934	0.058	0	0	−20.16	···	···	∞	∞	···	···
0.0850	12.000	1.0201	0.4883	3.914	0.3956	0.6963	−16	9.39	9.64	0.0869	0.0871	0.1032 (0.0174)	0.0086
0.08	12.758	1.0206	0.4890	3.907	0.3963	0.6960	−16	9.42	9.65	0.0819	0.0821	0.0972 (0.0176)	0.0077
0.07	14.441	1.0290	0.4905	3.912	0.3854	0.6971	−16	8.56	8.79	0.1542	0.1536	0.1829 (0.0150)	0.0272
0.06	16.398	1.0015	0.4917	3.996	0.3658	0.6898	−16	6.38	6.60	0.2648	0.2632	0.3151 (0.0119)	0.0815
0.05	18.619	0.9476	0.4929	4.186	0.3128	0.6914	−16	3.24	3.44	0.3968	0.3937	0.4765 (0.0090)	0.1899
0.04	21.028	0.8562	0.4938	3.373	0.1778	0.7236	−16	0.83	1.06	0.5425	0.5368	···	0.3960
0.03	23.461	0.7165	0.4946	1.295	0.0721	0.6602	−16	0.45	0.65	0.6921	0.6799	···	···
0.02	25.628	0.5218	0.4951	0.419	0.0263	0.4992	−16	0.39	0.42	0.8434	0.8048	···	···
0.00	27.710	0	0.4956	0.0585	0	0	−16	···	···	∞	∞	···	···
0.0808	10.905	0.8807	0.9834, 0.4822	3.084	0.3037	0.6304	−16	8.10	8.41	0.1022	0.1022	···	···

(ii) The energy emission starts decreasing exponentially (Fig. 7);
(iii) PN-based eccentricity estimates yield meaningless results (Table I);
(iv) The polarization becomes linear rather than circular (Fig. 6);
(v) The final angular momentum starts *decreasing*, rather than increasing, as P and L decrease (Fig. 8).

Binary mergers with $L \simeq L_{\rm crit}$ are those producing the largest Kerr parameter for the final black hole observed in our simulations, $j_{\rm fin} \simeq 0.724$. One is led to suspect that for maximally spinning holes having spins aligned with the orbital angular momentum, a large orbital eccentricity may lead to violations of the cosmic censorship conjecture. Using arguments based on the extrapolation of point-particle results (see also [57]), we conjecture that (1) the maximal Kerr parameter that can be obtained by any merger of nonspinning holes is not much larger than $j \simeq 0.724$, and (2) cosmic censorship will *not* be violated as a result of any merger, even in the presence of orbital eccentricity. Further numerical simulations are needed to confirm or disprove these conjectures.

The paper is organized as follows. We begin in Sec. II discussing to what extent the Newtonian concept of eccentricity can be generalized to characterize orbiting binaries in general relativity. For this purpose, we introduce and compare various PN estimates of the orbital eccentricity, and we show that these eccentricity estimates break down when the motion turns from inspiral to plunge. Sec. III is a brief introduction to the numerical code used for the simulations. After a discussion of the choice of initial data and of the code's accuracy, we show how reducing the orbital angular momentum affects the gravitational waveforms, the puncture trajectories and the polarization of the waves. In Sec. IV we study the multipolar energy distribution of the radiation and the angular momentum of the final Kerr black hole. In Sec. V we show that the salient features of our simulations can be understood using extrapolations of point-particle results. Sec. VI is devoted to fits of the ringdown waveform and to estimates of the energy radiated in ringdown waves. We conclude by considering possible future extensions of our investigation.

II. POST-NEWTONIAN ESTIMATES OF THE ECCENTRICITY

In Newtonian dynamics, the shape of a binary's orbital configuration is determined by two parameters, the semi-major axis and the eccentricity. These parameters are intimately tied to the binding energy and orbital angular momentum of the binary and our construction of sequences of binaries with increasing eccentricity is based on this Newtonian intuition. Specifically, we fix the binding energy of the system, progressively reduce the orbital angular momentum and thus produce a sequence of orbits of increasing eccentricity. Before doing so, however, we need to address a conceptual difficulty, namely, how to quantify eccentricity in general relativity.

It turns out, unfortunately, that there exists no unique, unambiguous definition of eccentricity in fully nonlinear general relativity. For this reason, in the following we will use PN arguments to quantify the initial eccentricity (or rather, *eccentricities*) of the simulations. We will consider in detail two different generalizations of the Newtonian eccentricity: the 3PN extension [58] of a quasi-Keplerian parametrization originally proposed by Damour and Deruelle [59], and a definition in terms of observable quantities recently introduced by Mora and Will [60].

A. Quasi-Keplerian parametrization

A quasi-Keplerian parametrization of eccentric orbits of objects with mass M_1 and M_2 has been derived at 1PN order in harmonic coordinates by Damour and Deruelle [59], extended to 2PN order in ADM coordinates by Damour, Schäfer and Wex [61,62] and completed to 3PN order by Memmesheimer *et al.* [58]. This 3PN parametrization gives the relative separation vector $\mathbf{r} = (r\sin\phi, r\cos\phi, 0)$ of the compact objects and the mean anomaly l as

$$r = a_r(1 - e_r \cos u), \tag{2.1a}$$

$$\frac{2\pi(\phi - \phi_0)}{\Phi} = v + (f_{4\phi} + f_{6\phi})\sin 2v + (g_{4\phi} + g_{6\phi}) \times \sin 3v + i_{6\phi}\sin 4v + h_{6\phi}\sin 5v, \tag{2.1b}$$

$$l \equiv \frac{2\pi(t - t_0)}{T} = u - e_t \sin u + (g_{4t} + g_{6t})(v - u) + (f_{4t} + f_{6t})\sin v + i_{6t}\sin 2v + h_{6t}\sin 3v, \tag{2.1c}$$

where u is the eccentric anomaly, $v = 2\arctan\{[(1 + e_\phi)/(1 - e_\phi)]^{1/2}\tan(u/2)\}$ and T is the orbital period. The key element in the parametrization, that makes it useful for comparisons with numerical results, is that the auxiliary functions a_r, e_r, Φ, $f_{4\phi}$, $f_{6\phi}$, $g_{4\phi}$, $g_{6\phi}$, $i_{6\phi}$, $h_{6\phi}$, $n = 2\pi/T$, e_t, g_{4t}, g_{6t}, f_{4t}, f_{6t}, i_{6t}, h_{6t} and e_ϕ can be expressed exclusively in terms of the binding energy $E_{\rm b}$, the total angular momentum L and the symmetric mass ratio η of the binary system. The complete expressions in terms of the dimensionless quantities $E \equiv E_{\rm b}/\mu$ and $h \equiv L/(\mu M)$ are listed in Eqs. (20) and Eqs. (25) of [58] for ADM-type and harmonic coordinates, respectively. Here $M = M_1 + M_2$ and $\mu = M_1 M_2/(M_1 + M_2)$ are the total and reduced mass of the system, respectively.

A comparison with the Newtonian accurate Keplerian parametrization

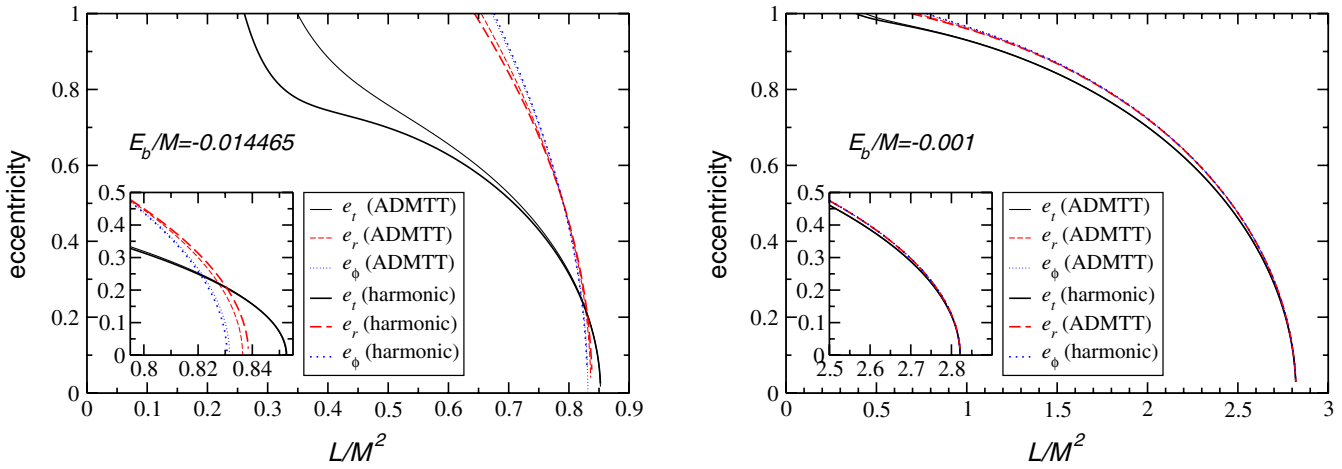

FIG. 1 (color online). The PN eccentricity parameters e_t, e_r and e_ϕ for an equal-mass binary with binding energy $E_{\rm b}$ are shown as functions of the orbital angular momentum L/M^2 for ADM-type coordinates and harmonic coordinates. The left panel shows the result for a binding energy corresponding to our sequence 1, the right panel that obtained for a much smaller binding energy.

$$r = a(1 - e\cos u), \tag{2.2a}$$

$$\phi - \phi_0 = 2\arctan\left[\left(\frac{1+e}{1-e}\right)^{1/2}\tan\frac{u}{2}\right], \tag{2.2b}$$

$$l = u - e\sin u, \tag{2.2c}$$

illustrates that the concept of eccentricity is much more complex in general relativity and a single number, such as the Newtonian eccentricity e, no longer suffices to parametrize the shape of the orbit. Nevertheless, the similarity of the Newtonian and 3PN expressions suggest that the numbers e_t, e_r and e_ϕ represent some measure of the deviation of the binary's orbit from quasicircularity. This becomes particularly clear if we plot these quantities as functions of the orbital angular momentum L/M^2 for fixed binding energy $E_{\rm b}/M$ and mass ratio η.

The result obtained for our sequence 1 models is shown in the left panel of Fig. 1. Several features of this plot are noteworthy. First, all eccentricity parameters diverge in the limit of a head-on collision. This is an artifact of the appearance of $1/(-2Eh^2)$ terms in the PN expressions for e_t, e_r and e_ϕ in Eqs. (20) and (25) of Ref. [58]. We note that the limit $L \to 0$ also plays a special role in the Newtonian case. The usual distinction between the range $0 \le e < 1$, corresponding to bound elliptic orbits, and $e \ge 1$, corresponding to unbound parabolic or hyperbolic trajectories, no longer applies in the case of vanishing angular momenta. Since in Newtonian theory

$$e^2 = 1 + f(M_1, M_2)E_b L^2, \tag{2.3}$$

where $f(M_1, M_2)$ is a function of the masses, in the head-on limit we would formally have $e = 1$, irrespective of the sign of the binding energy. Indeed such trajectories only have one degree of freedom, the energy, and the concept of eccentricity no longer applies. In this sense, it is not surprising that the PN formalism fails to provide meaningful values for e_t, e_r and e_ϕ in the head-on limit.

The second observation to be made is the steep gradient of all eccentricity parameters close to the circular limit of vanishing e_t, e_r and e_ϕ. The strong sensitivity of these parameters to the orbital angular momentum L results in finite values of the three eccentricities (of about 0.1) even when using quasicircular parameters, as obtained from Eq. (65) of Ref. [14]. Similarly, we observe that e_t, e_r and e_ϕ do not vanish for the same values of L (see the inset in the left panel of Fig. 1). Instead, the values of e_t and e_r corresponding to the orbital angular momentum where e_ϕ vanishes are of the order of 0.1. A similar uncertainty results from comparing the PN values obtained in harmonic and Arnowitt-Deser-Misner transverse traceless (ADMTT) coordinates (cf. the results in the two gauges in the left panel). We thus take 0.1 as an approximate lower limit for these eccentricity parameters obtainable for such relatively large binding energies using the 3PN Keplerian parametrization. This is also approximately the value of e_t, e_r and e_ϕ obtained for the quasicircular configurations of Table I.

A third noteworthy feature of the "quasi-Keplerian" PN parametrization (2.1) is its breakdown for close, near-merger binary orbits. For example, if we tried to compute e_r and e_ϕ for the "almost circular" parameters we use in this paper (as listed in Table I) they would turn out to be imaginary when, roughly speaking, $P/M \gtrsim 0.10$ (or $L/M^2 \gtrsim 0.83$). This is easy to understand by looking at the inset of the left panel of Fig. 1. There we see that these eccentricities have a zero crossing for values of L/M^2 which are *smaller* than those specified in our quasicircular simulations: in both ADMTT and harmonic coordinates, for the specified value of the binding energy e_r goes to zero when $L/M^2 \simeq 0.84$, and e_ϕ goes to zero when

$L/M^2 \simeq 0.83$. For L/M^2 larger than this "critical" value e_r^2 and e_ϕ^2 become negative, so that e_r and e_ϕ are imaginary. In the case of sequences 2 and 3, we observe the same behavior. This is just a sign that we should not trust the PN approximation for these highly relativistic configurations, so our eccentricity estimates should be taken with a grain of salt.

An eccentricity plot using the binding energy of sequence 2 or 3 would look almost indistinguishable from the plot for sequence 1, as shown in the left panel of Fig. 1, so we decided not to display them here. Instead, in the right panel of Fig. 1 we show the eccentricities computed for a much smaller binding energy, $E_b/M = -0.001$. This binding energy corresponds to a binary with much larger separation and smaller orbital velocity, that should be described with much higher accuracy by the quasi-Keplerian PN parametrization. In fact, in the Newtonian limit the three eccentricities should agree with each other, reducing to the Newtonian definition at large separations. For example, to leading PN order e_t and e_ϕ are related by

$$e_\phi = e_t[1 - (4 - \eta)(2\pi M/T)^{2/3}], \tag{2.4}$$

where T is the orbital period (see eg. [63]). The relation between the different eccentricities at higher PN orders can be found in Eq. (21) of Ref. [58].

From the right panel of Fig. 1 we see that the three eccentricity parameters do agree much better, as expected, when the binary members are far apart, and that differences resulting from the use of harmonic or ADMTT coordinates become negligible. We still see the breakdown of the formalism in the head-on limit. However, now all six curves are much closer to the expected Newtonian behavior, with vanishing eccentricity in the circular limit (where L approaches the maximum allowed value) and $e \approx 1$ for smaller angular momenta. Unfortunately, it is currently prohibitively costly from a computational point of view to start numerical simulations from such low binding energies. For this reason, in this paper we focus on the merger and ringdown signals resulting from eccentric binaries, rather than on detailed comparisons with PN predictions for the emission of GWs during the inspiral.

B. Mora-Will parametrization

An alternative estimate of the binary's initial eccentricity can be obtained using the PN diagnostic formalism developed by Mora and Will ([60], henceforth MW). Instead of imposing a quasi-Keplerian parametrization with different eccentricities for t, r and ϕ, MW define a *single* eccentricity parameter $e_{\rm MW}$ and a PN expansion parameter ζ as follows:

$$e_{\rm MW} \equiv \frac{\sqrt{\Omega_p} - \sqrt{\Omega_a}}{\sqrt{\Omega_p} + \sqrt{\Omega_a}}, \qquad \zeta \equiv \left(\frac{\sqrt{M\Omega_p} + \sqrt{M\Omega_a}}{2}\right)^{4/3}. \tag{2.5}$$

Here Ω_p and Ω_a are the orbital angular frequencies when the binary passes through a local maximum (pericenter) and through the next local minimum (apocenter), respectively.

The MW eccentricity parameter $e_{\rm MW}$ has several advantages: it is defined in terms of observable quantities, it reduces to its Newtonian counterpart for small orbital frequencies, and it is gauge invariant through first PN order. The binding energy and angular momentum of the system can be expressed as functions of $e_{\rm MW}$ and ζ. The relevant equations for black-hole binaries are given by Eqs. (2) and (3) in [64]. In Ref. [65] these same PN equations have been used to study truly eccentric black-hole binary initial data, and to point out some interesting features of the resulting effective potentials.

The PN expansion parameter ζ is related to the frequencies at periastron and apoastron by

$$\zeta = \frac{(M\Omega_a)^{2/3}}{(1 - e_{\rm MW})^{4/3}} = \frac{(M\Omega_p)^{2/3}}{(1 + e_{\rm MW})^{4/3}}. \tag{2.6}$$

To estimate the eccentricity, we can assume that the binary's orbit is (say) at apoastron, so that $\Omega = \Omega_a$. Then the binding energy and angular momentum can be expressed as functions of $e_{\rm MW}$ and $M\Omega$. We can equate these functions to the binding energies and angular momenta listed in Table I:

$$E_b^{\rm MW}(e_{\rm MW}, M\Omega) = E_b, \tag{2.7a}$$

$$L^{\rm MW}(e_{\rm MW}, M\Omega) = L. \tag{2.7b}$$

If our assumption is correct, and the orbit is indeed at apoastron, this system will have a solution $(e_{\rm MW}, M\Omega)$ with eccentricity $e_{\rm MW} > 0$. It should be obvious from Eq. (2.6) that a solution with $e_{\rm MW} < 0$ would simply correspond to the binary being at periastron.

In Ref. [64] it was shown that, when comparing numerically computed quasiequilibrium binary black-hole initial data against the MW PN diagnostic predictions *for a given orbital frequency* $M\Omega$, energies are usually in better agreement than angular momenta. Unfortunately, our initial data sets specify the orbital angular momentum and the binding energy, but not the orbital frequency. Therefore, to estimate the binary's eccentricity we adopt two different procedures. The first procedure is based on numerically solving the system (2.7) for the two unknowns $(e_{\rm MW}, M\Omega)$, which are both considered as free parameters. This procedure is quite general. However it can involve a significant amount of systematic error, since the angular momentum can deviate by a large amount from numerical initial data even for small eccentricities and/or large separations, and we are trying to solve for both energy and angular momentum simultaneously.

The second procedure is based on an assumption of quasicircularity, and it consists of two steps. We first assume that $e_{\rm MW} = 0$ and solve Eq. (2.7a) for $M\Omega$. For

sequence 1, the orbital frequency obtained by imposing $E_b^{\rm MW}(e_{\rm MW}=0, M\Omega)=E_b$ is $M\Omega=0.0513$; for sequence 2, we find $M\Omega=0.0431$; for sequence 3, we find $M\Omega=0.0212$. Then we substitute this value of $M\Omega$ in Eq. (2.7b) and solve for the eccentricity. We call this solution $e_{\rm MW,circ}$, because it is obtained assuming that the energy function is very close to the circular prediction, and that deviations of the eccentricity from zero only affect the angular momentum.

Table I lists the eccentricities e_t obtained using the definition by Memmesheimer *et al.* and the two eccentricities estimated from the MW diagnostic. Dotted entries mean that no solutions to the system (2.7) exist for physically relevant values of the parameters. The MW eccentricity estimate $e_{\rm MW}$ is consistent with the quasi-Keplerian parameter e_t: in fact, the two definitions are roughly in agreement, within factors of order unity. It is also encouraging that the minima of e_t and $e_{\rm MW}$ correspond to the same simulations along each sequence: these variables seem to provide a reasonably accurate measure of deviations from circularity, even for binaries which are very close to merger. The second procedure (by construction) should become inconsistent for large eccentricities, but $e_{\rm MW,circ}$ is much closer to the eccentricity estimates (~ 0.01) obtained in [64], and measured in longer quasi-circular inspiral simulations by different groups [21,66–68].

In the following we will use (somewhat arbitrarily) the parameter e_t obtained in harmonic coordinates as a measure of deviations from circularity of the initial binary configuration. We should still bear in mind that this parameter deviates significantly from the eccentricity e of a Keplerian ellipse, in particular, for small angular momenta.

III. NUMERICAL SIMULATIONS

The simulations presented in this work have been performed with the LEAN code [12], which is based on the CACTUS computational toolkit [69]. The code employs the so-called moving-puncture method, i.e. it evolves initial data of puncture type [70] using the Baumgarte-Shapiro-Shibata-Nakamura (BSSN) formulation of the Einstein equations and gauge conditions which allow the black holes to move across the computational domain. In contrast to the original version of the BSSN system, where the conformal factor ψ is evolved in the form of the logarithmic variable $\phi=\ln\psi$, we here evolve the variable $\chi=e^{-4\phi}$, as originally introduced in Ref. [7]. These equations are numerically approximated using fourth-order spatial discretization for sequences 1 and 2, and sixth-order spatial discretization [71] for sequence 3. Integration in time is performed with the method of lines using the fourth-order accurate Runge-Kutta (RK) scheme. Using the notation of Table 1 in Ref. [12], this corresponds to schemes labeled RK χ_4 and RK χ_6, respectively. We note, however, that neither version of the code is genuinely fourth- or sixth-order accurate, as second-order ingredients are used at the refinement and outer boundaries (see [12] for details).

The LEAN code facilitates use of mesh-refinement via the CARPET package [72,73]. Specifically, the computational grid is represented by a nested set of Cartesian boxes with resolution successively increasing by factors of two. The innermost refinement levels are typically split into two components centered around either hole and following the black-hole motion. Once the black-hole separation decreases below a threshold value, the two components merge into one centered around the origin. A more detailed description of the LEAN code is given in Ref. [12].

GWs are extracted using the Newman-Penrose formalism. The Newman-Penrose scalar Ψ_4 is calculated using the electromagnetic decomposition of the Weyl tensor, and decomposed into contributions of different multipoles using spherical harmonics $-2Y_{\ell m}$ of spin weight -2 according to

$$\Psi_4=\sum_{\ell,m-2} Y_{\ell m}\psi_{\ell m}. \tag{3.1}$$

For all simulations presented in this work we extract GWs at different extraction radii $r_{\rm ex}$. We use the results obtained at different radii to estimate the uncertainty arising from the use of a finite extraction radius.

The calculation of apparent horizons is performed using Thornburg's AHFINDERDIRECT [74,75] and plays an important role in the construction of initial data sequences.

We use initial data of puncture type as provided by Ansorg's TWOPUNCTURE thorn [76] in all simulations. For zero spins, an initial data set is uniquely determined by the bare mass parameters m_1 and m_2 of the holes, their initial coordinate separation D and the Bowen-York [77] parameters $\mathbf{P}_1$ and $\mathbf{P}_2$ for the black holes' linear momenta. Without loss of generality we always set $\mathbf{P}\equiv\mathbf{P}_1=-\mathbf{P}_2$. The initial orbital angular momentum is then given by $\mathbf{L}=\mathbf{D}\times\mathbf{P}$. Because the black holes are initially located on the x-axis and orbit in the xy-plane, the initial angular momentum is given by its z-component, which we can write as $L=L_z=DP$ (where $P=P_y$).

We conclude this brief description of the numerical code with a summary of the variables used in the remainder of this work. We denote by M_1 and M_2 the initial black-hole masses. The total mass is the sum of the individual masses, $M\equiv M_1+M_2$, and the reduced mass is $\mu\equiv M_1M_2/M$. We measure the mass ratio using either $q=M_1/M_2$ or the "symmetric mass ratio" parameter $\eta=\mu/M$ often used in PN studies. Finally, we denote the Arnowitt-Deser-Misner (ADM) mass by $M_{\rm ADM}$, which is close to (but in general different from) the total black-hole mass M. The normalization of dimensional quantities is performed as follows. Initial parameters are normalized using the total black-hole mass M for compatibility with the PN relations. In contrast, we measure radiated energy and momenta (as well as time t and radii r) in units of the ADM mass, as is

common in numerical studies. All normalizations will be clear from the use of M or $M_{\rm ADM}$ in column or axis labels; the relation between the two normalizations can be worked out from Eq. (3.2) below and from the binding energies of the two sequences we consider, which are given in the caption of Table I.

A. Sequence of initial data

The construction of a sequence of nonspinning, equal-mass binary initial configurations with constant binding energy is a two-step process. First, we determine a quasicircular configuration using the 3PN accurate relation (65) of Ref. [14], which provides the initial linear momentum P/M for given black-hole masses M_1 and M_2 and separation D/M. Without loss of generality we fix the scaling freedom of the numerical coordinates by setting $M_1 = M_2 = 0.5$. For fixed values of P and D, there thus remains the task of finding bare mass parameters $m_1 = m_2$ which result in black-hole masses of $M_1 = M_2 = 0.5$. This is done iteratively by using the Newton-Raphson method with initial guesses $m_i = M_i$. In the absence of spins, the black-hole masses are given by the irreducible masses, as calculated by the apparent horizon finder AHFINDERDIRECT. For the quasicircular model we calculate the binding energy according to

$$E_{\rm b} = M_{\rm ADM} - M. \tag{3.2}$$

The second step consists of the construction of additional configurations with the same binding energy but different linear momentum parameter P and, thus, different orbital angular momentum $L = DP$. For this purpose we fix P and demand, as before, $M_1 = M_2 = 0.5$. We then iteratively solve for the numerical parameters $m_1 = m_2$ and D which yield the required black-hole masses and binding energy.

Three sequences obtained this way with $E_{\rm b}/M = -0.014\,465$, $-0.013\,229$ and $-0.008\,861$ are listed in Table I. In the following we will refer to them as "sequence 1," "sequence 2" and "sequence 3," respectively. The corresponding quasicircular configurations are those with linear momentum $P/M = 0.1383$, 0.1247 and 0.0850.

It is worth mentioning, in this context, that our choice of fixing the binding energy is not unique. Alternative choices in constructing sequences include keeping constant the coordinate separations of the punctures, or the proper horizon-to-horizon distance. We have opted against these two options because they would result in very short merger times for small angular momenta. At constant binding energy, instead, smaller values of the orbital angular momentum imply larger separations of the holes and, thus, a delay in the formation of the common apparent horizon.

B. Accuracy of the simulations

In order to estimate the uncertainties associated with the numerically calculated quantities of sequences 1 and 2, we have performed a convergence analysis for the quasicircular configuration with $P/M = 0.1247$ of sequence 2, and for the eccentric configuration with $P/M = 0.08$ of sequence 1. We have evolved these systems using the following grid setup: $\{(192, 96, 56, 24, 12) \times (3, 1.5, 0.75), h_i\}$. By this notation we mean that there is a total of 8 refinement levels. The 5 outer levels are centered on the origin and extend out to $x = y = z = \pm 192$, 96, 56, 24 and 12, respectively. The 3 inner levels have 2 components each, centered on either hole with radius 3, 1.5 and 0.75. Finally, the grid spacing is h_i on the finest level (where $h_1 = 1/48$, $h_2 = 1/44$ and $h_3 = 1/40$) and increases by a factor of 2 consecutively on each level.

Fourth-order convergence is shown in Fig. 2 for the ($\ell = 2, m = 2$) multipole of the Newman-Penrose scalar Ψ_4, the total radiated energy E and the radiated angular momentum in the z-direction $J_{\rm rad}$.

Using the fourth-order convergence, we apply a Richardson extrapolation to the total radiated energy and obtain $E/M_{\rm ADM} = 0.036\,86$, $0.036\,68$ and $0.036\,56$, respectively, at extraction radii $r_{\rm ex}/M_{\rm ADM} = 50.7$, 60.8 and 70.9. These values correspond very well to a $1/r_{\rm ex}$ falloff of the uncertainty arising from the use of finite extraction radii. The total radiated energy extrapolated to $r_{\rm ex} \to \infty$ is $E/M_{\rm ADM} = 0.035\,83$. For the medium resolution case ($h = h_2 = 1/44$) and using an extraction radius $r_{\rm ex}/M_{\rm ADM} = 70.9$, this analysis predicts an uncertainty $\sim 2\%$ due to the discretization and $\sim 2.5\%$ due to the use of finite extraction radius. The uncertainties in the radiated angular momentum $J_{\rm rad}$ are $\sim 2\%$ for both error sources. The convergence study of the eccentric simulation with $P/M = 0.08$ of sequence 1 yields similar error estimates. We estimate the resulting total error from quadratic error propagation to be about 3%. In fact, this estimate is likely to be very conservative because the two error sources have opposite signs: finite resolution tends to underestimate radiated energy and momenta, while finite extraction radius usually leads to an overestimate.

Performing a convergence analysis of simulations lasting as long as those of sequence 3 requires vast computational resources. In order to reduce the cost, we view these simulations as part of a wider parameter study, to be presented elsewhere, which also involves unequal-mass binaries. In order to assess the accuracy of those long simulations, we have focused on a quasicircular configuration with $q = 2$ which is listed as the last entry in Table I. From experience, we consider unequal-mass binaries significantly more challenging numerically than systems with equal mass, and therefore feel justified in using the uncertainties resulting from this model as conservative error estimates of our sequence 3 runs. We have evolved this configuration using a grid $\{(384, 192, 128, 48, 24) \times (6, 3, 1.5, 0.75), h_i\}$ with $h_i = 1/44$, $1/48$ and $1/56$. The bottom panels of Fig. 2 show the convergence of the phase and amplitude of Ψ_4 (bottom right panel) and the radiated

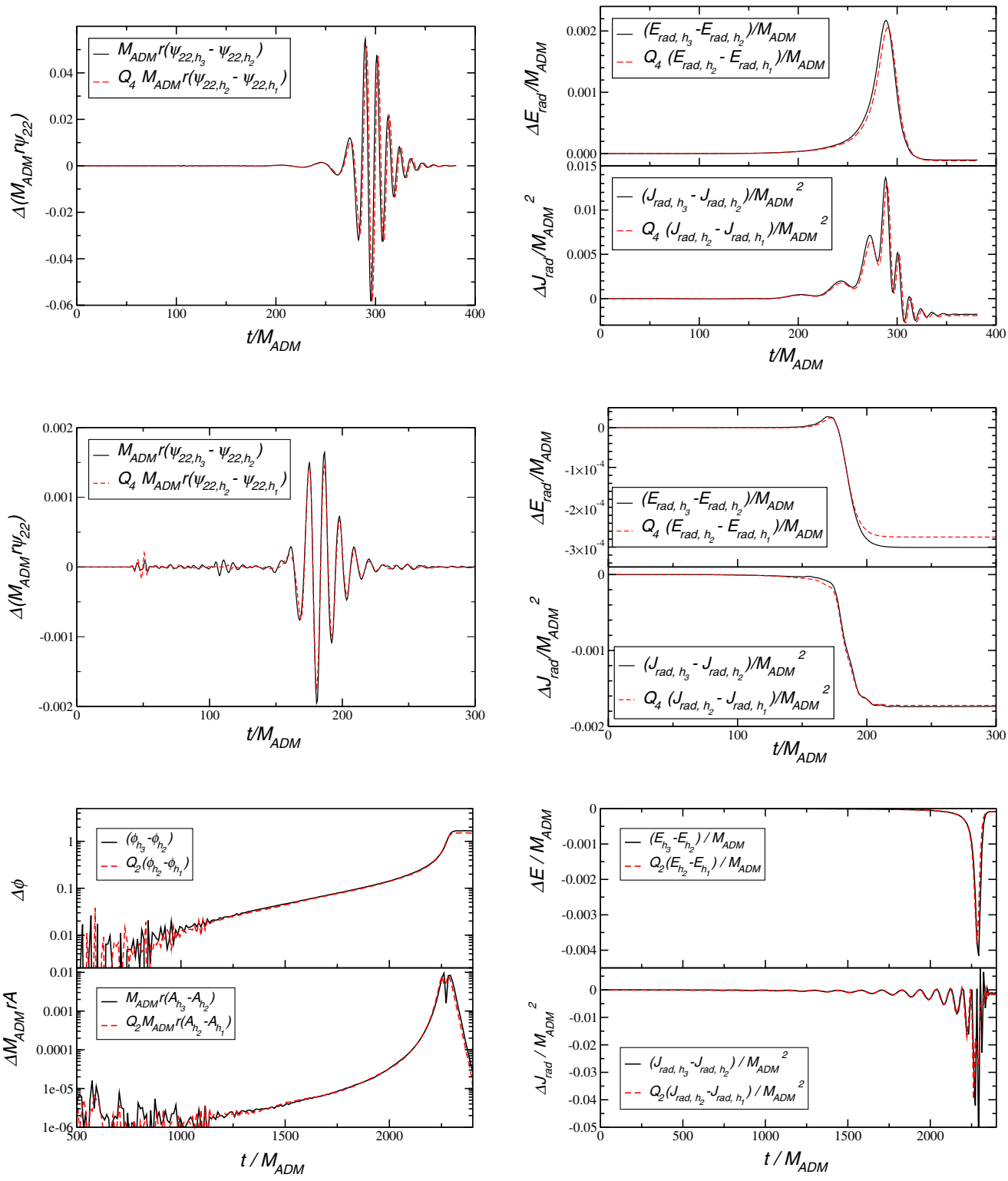

FIG. 2 (color online). Upper panels: convergence analysis of the $P/M = 0.1247$, quasicircular model of sequence 2, using resolutions $h = 1/48$, $1/44$ and $1/40$. The left panel shows the differences in the ($\ell = 2$, $m = 2$) multipole of $M_{\rm ADM} r\psi_{22}$, the right panel the total radiated energy and z-component of the angular momentum. In both cases, the differences between the higher resolution simulations have been rescaled by Q_4 for the expected fourth-order convergence. Middle panels: same, but for the $P/M = 0.08$, eccentric model of sequence 1. Lower panels: same, but for the unequal-mass model listed at the bottom of Table I. For clarity, we present the convergence of Ψ_4 using phase and amplitude instead of the real part. For this configuration, we observe second-order convergence. The corresponding convergence factors for the resolutions used here are $Q_4 = 1.58$ and $Q_2 = 0.72$.

energy and angular momentum (bottom left panel). The difference between the higher resolution runs has been rescaled for second order convergence. We observe second-order convergence for these runs except for the late stages near merger, when the convergence increases to third order. Similar glitches in the convergence near merger have been observed in [20]. Using the same technique as above, we obtain uncertainties of about 3% for the radiated energy and 6% for the radiated angular momentum for the simulations using $h_2 = 1/48$ and $r_{\rm ex} = 80.7 M_{\rm ADM}$.

Because most simulations have been performed at the medium resolution only, we cannot in general apply Richardson extrapolation. Unless specified otherwise we therefore present results as obtained numerically using $h = 1/44$ and $r_{\rm ex}/M_{\rm ADM} = 70.9$ for sequences 1 and 2, as well as $h = 1/48$ and $r_{\rm ex} = 120M$ for sequence 3, bearing in mind the uncertainties we have just mentioned.

We conclude this discussion by mentioning that the LEAN code has been demonstrated to accurately evolve black holes with large spins in Ref. [78]. Specifically, methods to calculate the spin from quasinormal ringing, balance arguments and apparent horizon data were shown to result in excellent agreement for Kerr parameters above 0.9.

C. Numerical waveforms

In Ref. [22] we studied the multipolar energy distribution of unequal-mass black-hole binaries in quasicircular orbits. By projecting 2.5 PN calculations of the inspiral gravitational waveforms onto spin-weighted spherical harmonics ${}_{-2}Y_{\ell m}$, we concluded that odd-m multipoles of the radiation are suppressed for equal-mass binaries. Low-ℓ multipoles carry most of the radiation, and within a given l-multiplet, modes with $\ell = m$ are typically dominant for quasicircular motion. This analytical prediction was shown to agree very well with numerical simulations, and it has recently been confirmed by more accurate PN calculations [79]. Since in this paper we study equal-mass runs, we expect even-m, low-ℓ multipoles to be dominant, at least

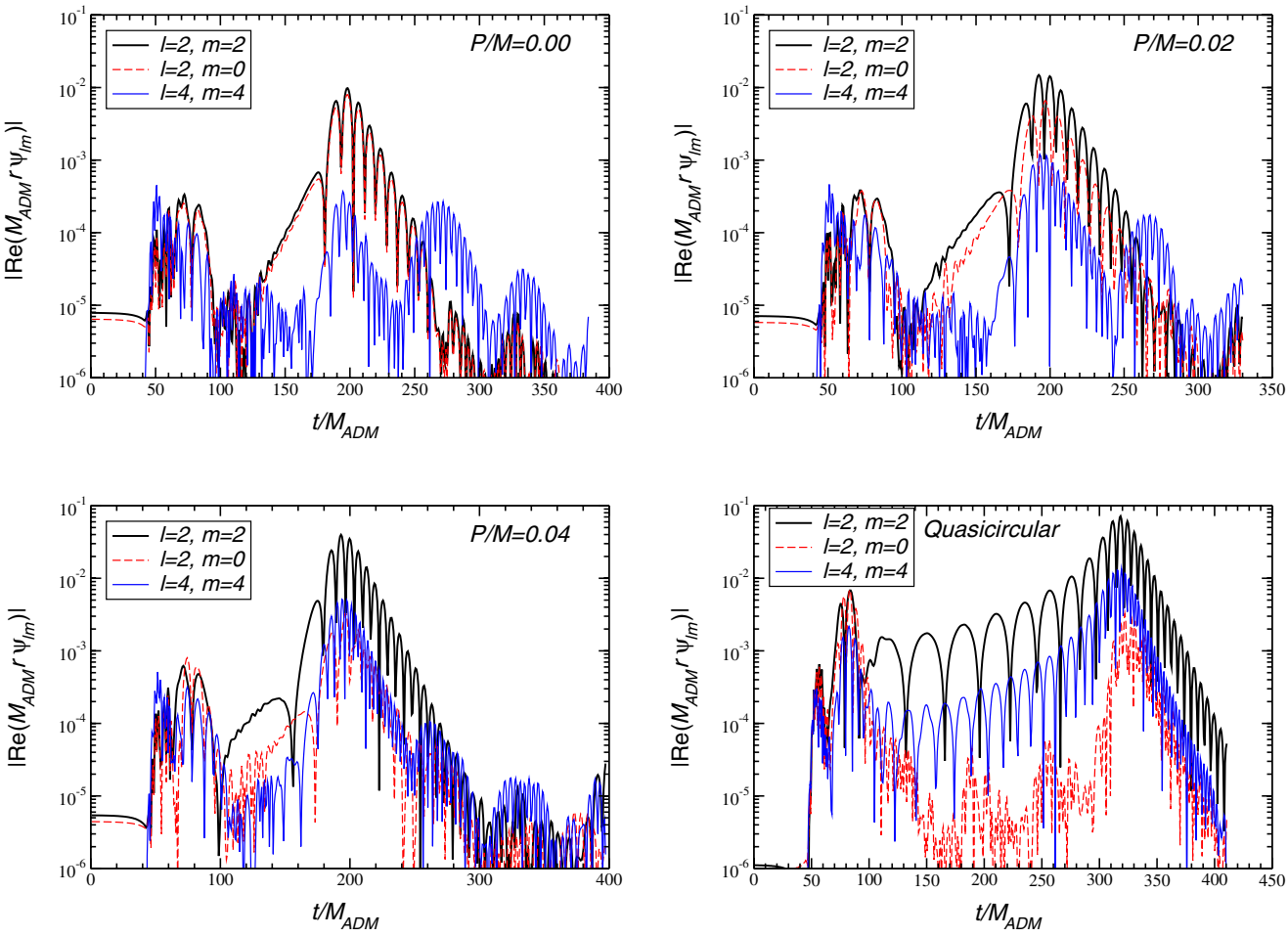

FIG. 3 (color online). Modulus of the real part of the ($\ell = 2$, $m = 2$), ($\ell = 2$, $m = 0$) and ($\ell = 4$, $m = 4$) components of the waveforms. We show waveforms from four representative simulations: sequence 2 runs with $P/M = 0$ (head-on limit), $P/M = 0.02$, $P/M = 0.04$ and $P/M = 0.1247$ (quasicircular case).

when the eccentricity is small enough. This expectation is again confirmed by our numerical time evolutions.

To be more quantitative, in Fig. 3 we show the modulus of the real part of the ($\ell = 2$, $m = 2$), ($\ell = 2$, $m = 0$) and ($\ell = 4$, $m = 4$) components of the Weyl scalar for some representative runs. From these plots it is clear that the ($\ell = 2$, $m = 0$) component contributes significantly for $P/M \lesssim 0.05$. That the ($\ell = 2$, $m = 0$) component should be significantly excited in the head-on limit $P/M \to 0$ is known from previous numerical simulations: in fact, the $m = 0$ mode would by far be dominant if we had chosen the collision to happen along the z-axis (see e.g. [80,81]). Notice that in this paper GWs have always been extracted assuming that the z-axis is perpendicular to the orbital plane. In the case of head-on collisions this is contrary to most previous studies, where to take full advantage of the symmetry of the problem the axis of reference for the angular coordinates is identified with the axis of collision. In consequence, we find the radiated energy of head-on collisions to be quadrupole dominated, but to contain $m = \pm 2$ and $m = 0$ contributions of comparable magnitude rather than almost exclusively an $\ell = 2$, $m = 0$ contribution as is the case for alignment of the two axes. Our choice is entirely motivated by using identical angular coordinates throughout the sequence of models. A detailed analysis of the transformation properties of multipolar components of the radiation under rotations, translations and boosts can be found in Ref. [82].

As P/M increases and we approach quasicircular motion, the low-amplitude portion of the ($\ell = 2$, $m = 0$) mode decreases in amplitude, and it is significantly contaminated by noise. As expected from our previous study [22], in the same limit the amplitude of the ($\ell = 4$, $m = 4$) mode grows. Unfortunately, Fig. 3 illustrates that even for ($\ell = 4$, $m = 4$), which is the largest of the subdominant radiation modes, the ringdown signal is strongly distorted by either nonlinear effects or boundary reflection noise. For this reason it is difficult to use higher multipoles to improve spin estimates from quasinormal mode (QNM) fittings, as proposed in [22]. This problem will be discussed in more detail in Sec. VI below.

We can obtain an estimate of the number of orbits in our simulations from the puncture trajectories, calculated according to $dx^i/dt = -\beta^i$. For illustration, in Fig. 4 we plot the trajectories of four models of sequence 2 with $P/M =$ 0.02, 0.06, 0.10 and 0.1247. The figure demonstrates the inspiraling nature of the simulations with large initial momentum, whereas those with small momentum rather represent plunging configurations.

We define a phase $\phi_{\rm punc}$ of these trajectories by expressing the puncture's position in spherical polar coordinates

$$(x, y) = (r_{\rm punc}\cos\phi_{\rm punc}, r_{\rm punc}\sin\phi_{\rm punc}). \qquad (3.3)$$

Then we consider the phase difference $\Delta\phi_{\rm punc} = \phi_{\rm punc}(t_{\rm cah}) - \phi_{\rm punc}(t_0)$, where $t_{\rm cah}$ is the time of formation

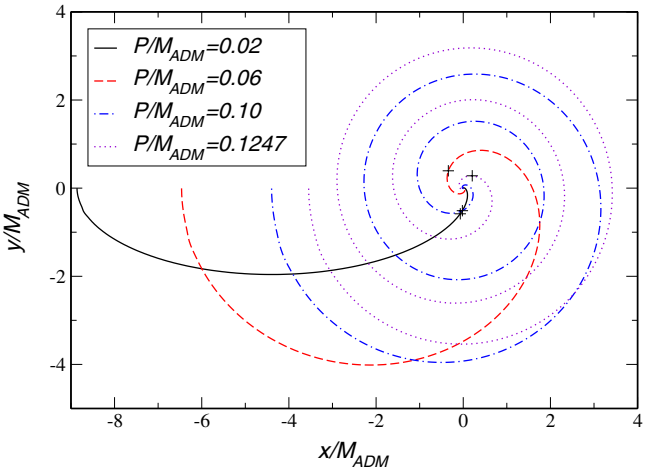

FIG. 4 (color online). Trajectories of the models with $P/M =$ 0.02, 0.06, 0.10 and 0.1247 of sequence 2. The trajectory of one hole only is shown in each case. The positions of the respective second holes follow from symmetry across the origin. The + denote the locations of the individual holes at the time of common apparent horizon formation.

of a common apparent horizon and we choose $t_0 = 50M_{\rm ADM}$ to cut off the initial data burst (this is consistent with the derivation of the frequency from the GW signal, discussed below). The number of orbits then follows from $N_{\rm punc} = \Delta\phi_{\rm punc}/(2\pi)$.

The gravitational wave signal Ψ_4 also serves to estimate the number of orbits completed by the binary prior to merger. For this purpose we focus on the ($\ell = 2$, $m = 2$) multipole and decompose the mode coefficient into a time-dependent amplitude $A(t)$ and phase $\phi(t)$ according to

$$\psi_{22}(t) = A(t)e^{i\phi(t)}. \qquad (3.4)$$

We next calculate the phase difference

$$\Delta\phi = \phi(t_{\rm cah} + r_{\rm ex}) - \phi(t_0 + r_{\rm ex}), \qquad (3.5)$$

where $r_{\rm ex}$ takes (approximately) into account the time it takes for the waves to propagate to the extraction radius. The number of orbits completed by the binary is then estimated as $N_{\rm waves} = \Delta\phi/(4\pi)$, where the additional factor of 2 compensates for the difference between the orbital frequency and that of a multipole with $m = 2$. Both estimates of the number of orbits, together with the time of formation of the common apparent horizon, are given in Table I. Small differences in these numbers are due to the fact that the approximate relation $\omega_{\rm waves} = m\omega_{\rm punc}$ breaks down near the merger of the holes.

This is illustrated in Fig. 5. There we plot the frequency ω_{22} and the phase ϕ_{22} obtained from ψ_{22}, comparing with the frequency $m\omega_{\rm punc}$ and phase $\phi_{\rm punc}$ obtained from the puncture trajectory (see [22] for details). Estimates from the punctures' motion are physically irrelevant after formation of the apparent horizon. The upper panels refer to

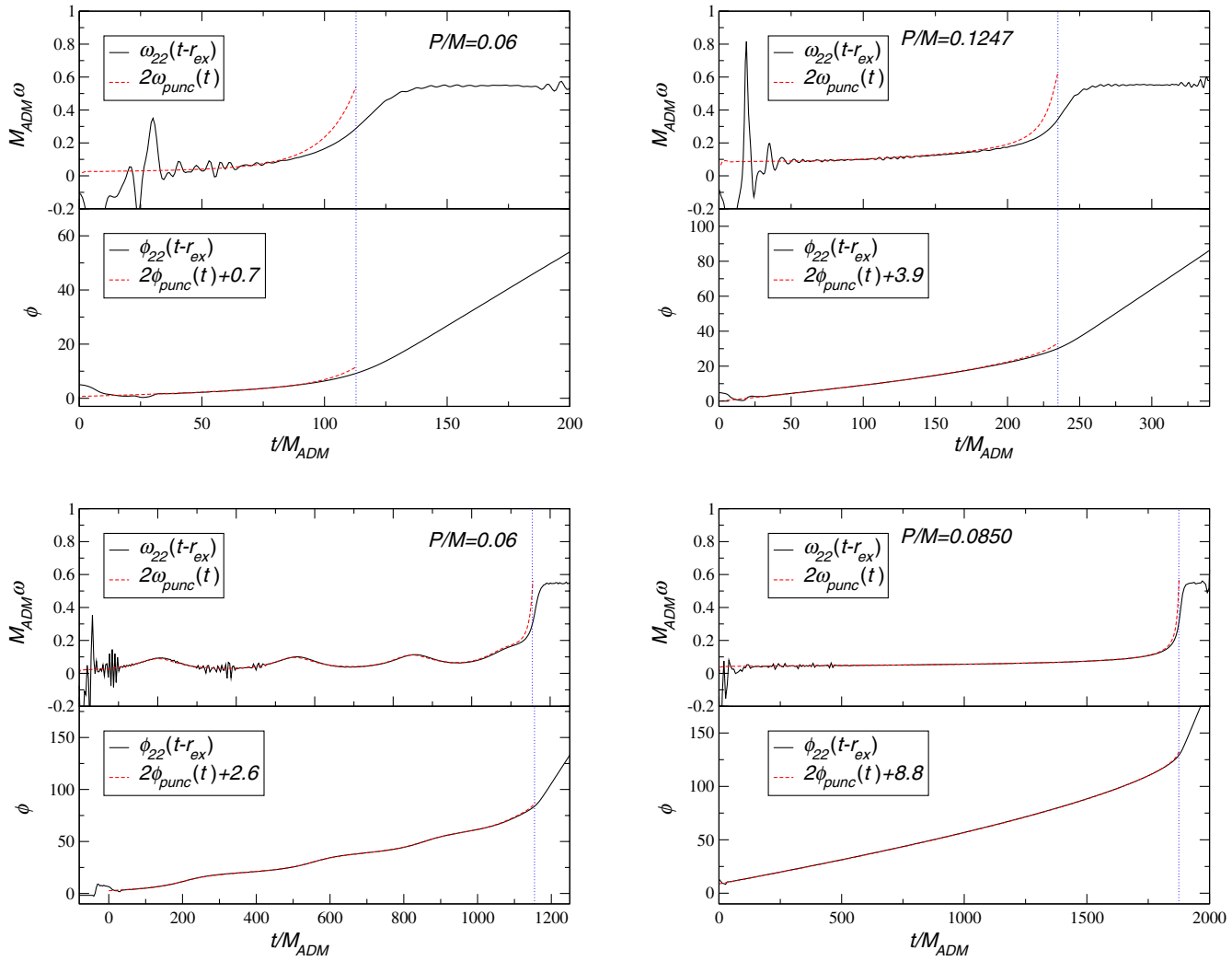

FIG. 5 (color online). Frequency and phase obtained from the $\ell = 2$, $m = 2$ multipole of the gravitational radiation as well as the puncture trajectory for models $P/M = 0.06$ and 0.1247 of sequence 2 (upper panels) and $P/M = 0.06$ and 0.0850 of sequence 3 (lower panels). The dotted vertical lines mark the formation of the apparent horizon.

different models from sequence 2: a nearly plunging motion with $P/M = 0.06$ (left) and a quasicircular orbit with $P/M = 0.1247$ (right). It is clear from the figure that deviations between $\omega_{\rm waves}$ and $m\omega_{\rm punc}$ grow significantly near merger. The same holds for the two models of sequence 3 shown in the bottom panels.

From Fig. 4, and from the data for $N_{\rm punc}$ and $N_{\rm waves}$ listed in Table I, we deduce that the simulations with $L \lesssim L_{\rm crit} \simeq 0.08M^2$ complete significantly less than one cycle, so they are effectively plunging trajectories. Consistently with this interpretation, we have seen in Sec. II below that PN estimates of the eccentricity of the orbit fail for these plunging configurations.

D. Polarization

In Appendix D of [22] we proposed to measure the polarization of a waveform using an "elliptical component of polarization" P_E. This quantity has the property that $P_E = 1$ for circular polarization, and $P_E = 0$ for linear polarization. By looking at the dominant ($\ell = 2$, $m = 2$) component of the radiation we also showed that, with the exception of the (unphysical) initial data burst and of the final part of the signal, which is dominated by noise, the polarization of a binary moving in a quasicircular orbit is circular to a very good approximation.

In Fig. 6, to be compared with Fig. 28 of Ref. [22], we show the real and imaginary parts of the dominant ($\ell = 2$, $m = 2$) multipolar component of the radiation emitted by equal-mass binaries with different values of P/M as obtained from our sequence 2. In the bottom panel of each plot we compute the elliptical component of polarization. The results clearly illustrate that the polarization is linear in the head-on limit, where the imaginary component of the radiation vanishes, and that $P_E \to 1$ as the orbit becomes circular. It is also worth noticing that the ringdown part of

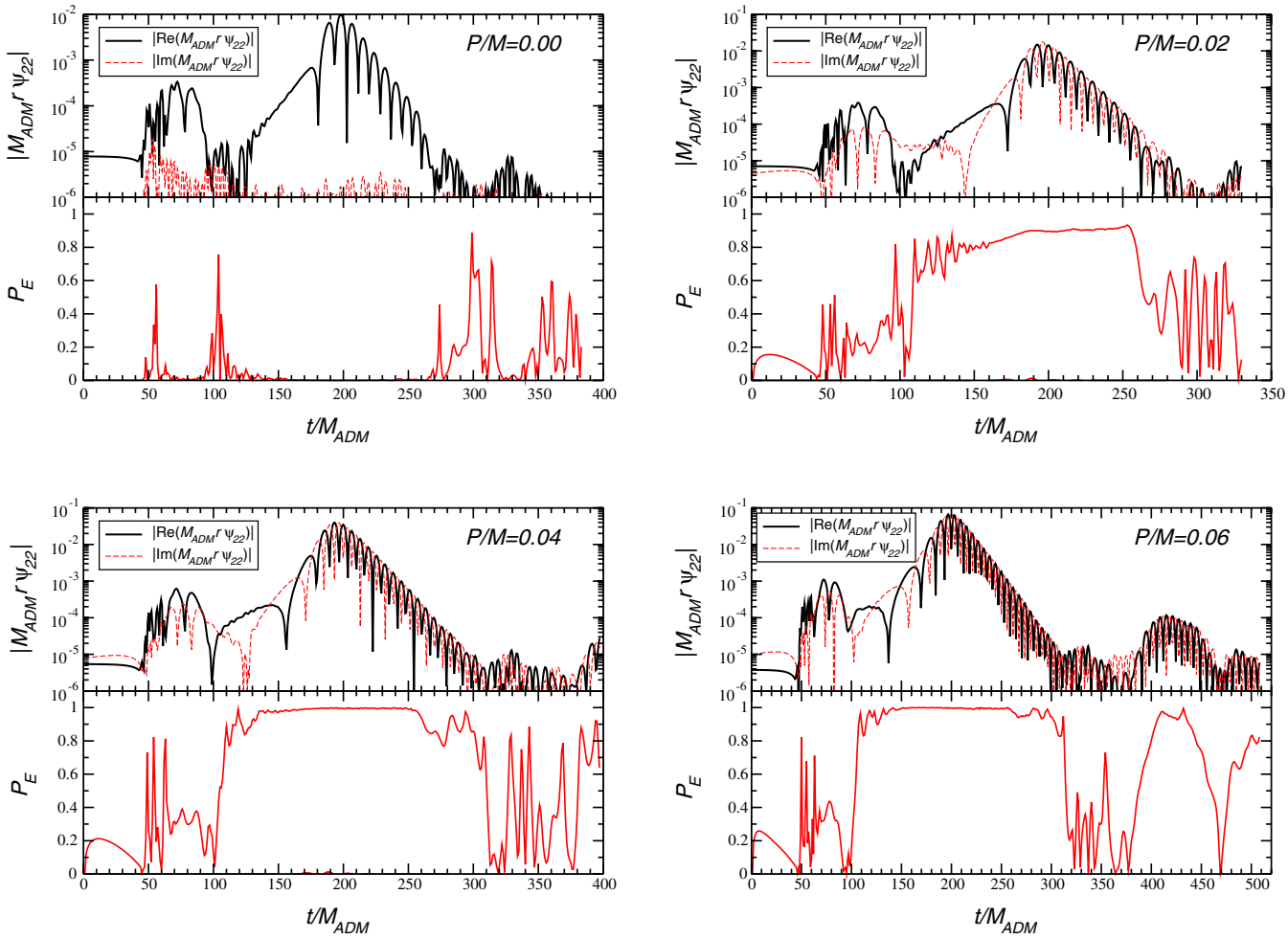

FIG. 6 (color online). $\ell = m = 2$ components of the low-L (or low-P) waveforms and their polarization for various models of sequence 2. For $L = 0$ the imaginary part of the waveform is zero within the noise level (i.e., the cross component is zero for symmetry reasons). As L increases, the polarization becomes circular. Spikes in P_E at early times are due to the initial data burst, and spikes at late times are due to boundary reflection noise and low strength of the signal.

the signal is circularly polarized even when P_E is slightly less than one in the inspiral part (see e.g. the plot for $P/M = 0.02$).

IV. RADIATED ENERGY AND FINAL ANGULAR MOMENTUM

In this section we study the multipolar energy distribution and the final angular momentum for the three sequences of simulations listed in Table I.

The multipolar distribution of radiated energy for sequence 1 is shown in the upper left panel of Fig. 7. We have excluded radiation due to the initial burst by ignoring contributions at simulation times $t < 50M + r_{\rm ex}$. The results demonstrate a relatively weak dependence of the radiated energy in each multipole on initial linear momenta $P/M \gtrsim 0.08$, corresponding to an angular momentum of $L/M^2 \sim 0.8$.

For smaller linear (or angular) momenta, we observe that: (1) the total radiated energy decreases almost exponentially, (2) the relative contribution of multipoles with $\ell > 2$ becomes weaker, and (3) the contribution of the ($\ell = 2$, $m = 0$) mode increases to approximately the same level as the ($\ell = 2$, $m = \pm 2$) modes. All of these features are quite insensitive to the inclusion of the spurious initial wave burst: only the ($\ell = 2$, $m = 0$) mode is significantly contaminated by the initial radiation when $P/M \gtrsim 0.08$. The same observations also apply to the models of sequence 2, shown in the right panel of Fig. 7. Here the transition seems to occur at a linear momentum slightly below $P/M = 0.08$. From Table I we see that this again corresponds to an angular momentum of $L/M^2 \approx 0.8$. Similarly, the transition occurs just below $P = 0.04$ in the case of sequence 3, which again corresponds to an orbital angular momentum $L/M^2 \approx 0.8$. A fit of sequence 1 runs by a polynomial in L/M^2 yields

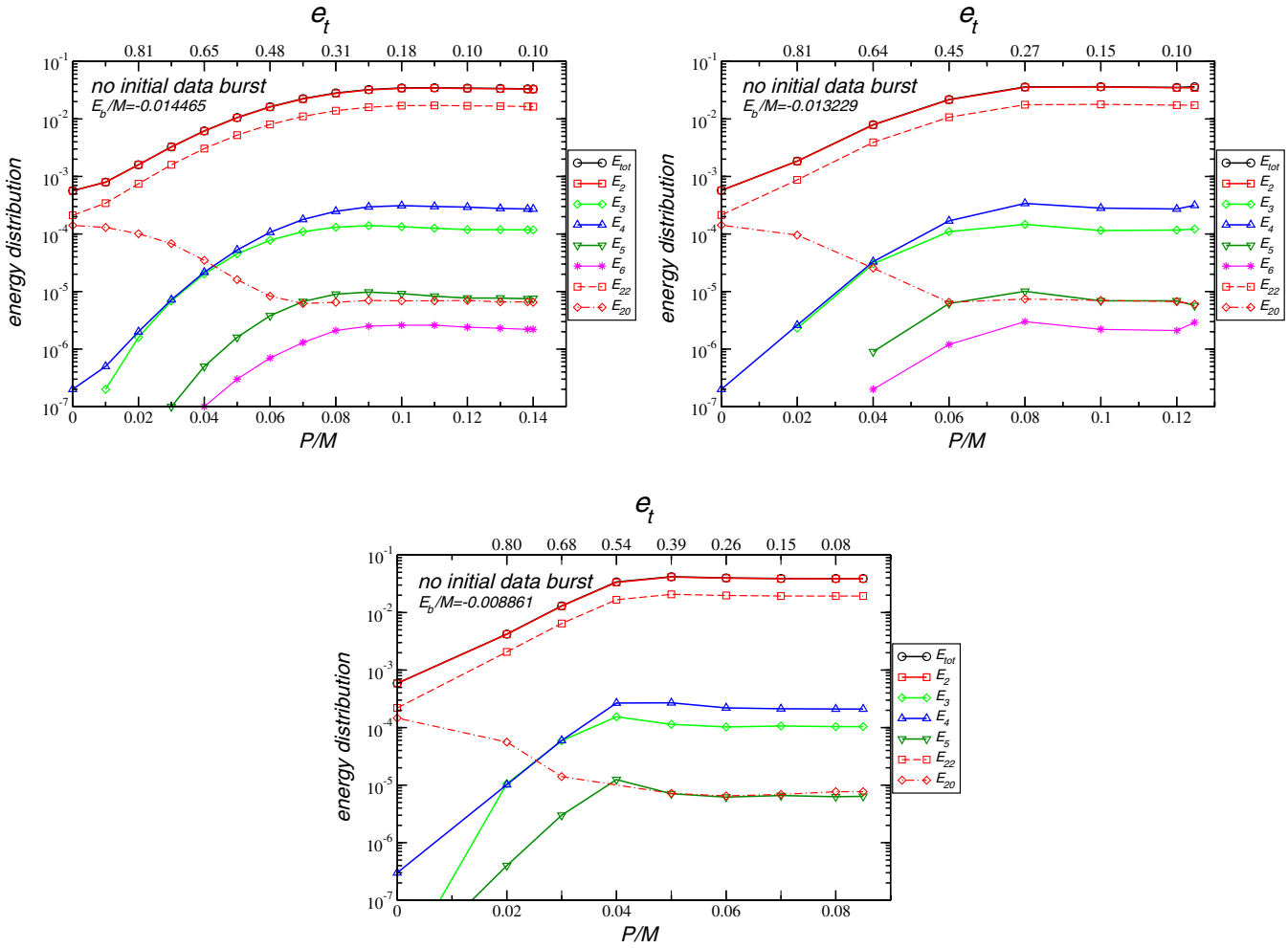

FIG. 7 (color online). Multipolar energy distribution as a function of the initial momentum P for sequence 1 (upper left), sequence 2 (upper right) and sequence 3 (lower). E_ℓ denotes the energy radiated in all multipoles with indices ℓ and $m = -\ell, \ldots, \ell$. We remove the initial data burst by ignoring all data with $t < r_{\rm ext} + 50M$.

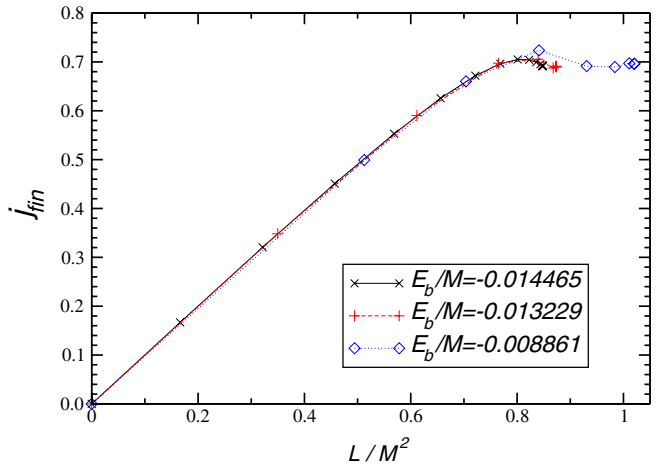

FIG. 8 (color online). Final angular momentum as a function of the initial momentum P for sequence 1 (solid line, crosses), 2 (dashed line, plus) and 3 (dotted line, diamonds).

$$\frac{E_{\rm rad}}{M_{\rm ADM}} = 0.0212\left(\frac{L}{M^2}\right) - 0.1020\left(\frac{L}{M^2}\right)^2 + 0.1478\left(\frac{L}{M^2}\right)^3. \tag{4.1}$$

A similar behavior is found for the angular momentum of the final black hole, shown in Fig. 8. We have calculated the final spin from balance arguments: the final black-hole mass $M_{\rm fin}$ is obtained by subtracting the total radiated energy from the initial ADM mass, and the final black-hole angular momentum $J_{\rm fin}$ is similarly given by the initial orbital angular momentum minus the momentum radiated in GWs. The figure shows the dimensionless Kerr parameter $j_{\rm fin} = J_{\rm fin}/M_{\rm fin}^2$. Again, small increases in eccentricity only lead to a mild increase in the final spin. The Kerr parameter has a local maximum, and then it decreases rapidly for $L/M^2 \lesssim 0.8$. The results for the three sequences show remarkably good agreement below $L/M^2 \lesssim 0.8$ and merely differ at large angular momenta, as initial

configurations with such large L only exist when choosing sufficiently large separations. By experimenting with sequence 1 runs, we found the following, reasonably accurate three-parameter polynomial fit:

$$\frac{J_{\rm rad}}{M_{\rm ADM}^2} = 0.0225\left(\frac{L}{M^2}\right) + 0.0381\left(\frac{L}{M^2}\right)^2 + 0.5589\left(\frac{L}{M^2}\right)^7. \tag{4.2}$$

The large exponent in the final term is an artifact of the phenomenological nature of the fit and yields optimal agreement with the data. We found that the following alternative fitting functions, with two unknowns, also perform very well, yielding $E_{\rm rad}/M_{\rm ADM} = 3.18 \times 10^{-4} \times e^{5.54L/M}$ and $J_{\rm rad}/M_{\rm ADM}^2 = 7.34 \times 10^{-4} e^{6.74L/M}$.

An understanding of the apparent threshold in the orbital angular momentum L/M^2 separating inspiraling and plunging orbits can be obtained by considering geodesic orbits in a Schwarzschild background. The key observation here is that particles of mass m_p in closed orbits must satisfy the condition $L/m_p > 2\sqrt{3}M$. A rough extrapolation of this result to comparable-mass binaries would yield $L/(\eta M) > 2\sqrt{3}M$, or $L/M^2 > 0.866$. There is no firm theoretical justification for this extrapolation, and yet the point-particle threshold $L/M^2 = 0.866$ is remarkably close to the observed transition range of $L/M^2 \approx 0.8$.

The agreement gets even better if, in the spirit of Ref. [57], we use a slightly improved perturbative model, considering particle orbits around a Kerr black hole with spin given by the final Kerr parameter of our simulations (see Sec. V and the appendix for details). For eccentric inspirals, the minimum allowed angular momentum should be attained at the so-called *separatrix* corresponding to the maximal allowed eccentricity, $e_p = 1$, where e_p is the eccentricity defined in Eq. (A6) for point-particle geodesics. The orbital angular momentum at the separatrix is also a function of the final black hole's spin, $L_{\rm sep}(j_{\rm fin}, e_p)$, and it is defined below in Eq. (5.1). An explicit calculation yields striking agreement with numerical simulations: $L_{\rm sep}(j_{\rm fin} = 0.69, e_p = 1) = 0.778M^2$ when we consider the final spin $j_{\rm fin} = 0.69$ produced by a quasicircular inspiral, and $L_{\rm sep}(j_{\rm fin} = 0.724, e_p = 1) = 0.763M^2$ when the final hole has the largest spin observed in our simulations.

Our interpretation of this similarity is that simulations with $L/M^2 \lesssim 0.8$ can no longer be viewed as eccentric orbiting black-hole binaries, but rather represent plunging configurations or grazing collisions. The change in character of the energy distribution visible in Fig. 7 when $L/M^2 \approx 0.8$ thus demonstrates the transition from orbiting to plunging binary systems.

Our simulations starting at different initial separation show some degree of universality in this transition. This can be understood in terms of the relatively low amount of angular momentum the binaries emit in the earlier stages of the inspiral (or plunge). In fact, consider some arbitrary configuration of sequence 3 with binding energy $E_{\rm b}^{(3)}/M = -0.008\,861$. As the binary evolves, it emits gravitational radiation and the binding energy decreases. Of particular interest for our argument is the moment in time when the binding energy decreases to the value $E_{\rm b}^{(2)}/M = -0.013\,229$ corresponding to sequence 2. In order to estimate this time, we consider the radiated energy $\Delta E_{\rm rad}(t)$ measured at $r_{\rm ex}$, integrated up to time t. The *transition time* t_{32} from sequence 3 to sequence 2 is then approximated by the relation

$$\Delta E_{\rm rad}(t_{32} + r_{\rm ex}) = E_{\rm b}^{(3)} - E_{\rm b}^{(2)}. \tag{4.3}$$

We next calculate the total amount of angular momentum $\Delta J_{\rm rad}/M_{\rm ADM}^2(t_{32} + r_{\rm ex})$ radiated away by the system during its transition from sequence 3 to sequence 2. The same procedure is applied for the transition from sequence 2 to 1. Results are shown in Table II.

By comparison with the initial orbital angular momentum L/M^2 listed in the third column of Table I we see that all binary models starting with orbital angular momentum near the critical value $L/M^2 \simeq 0.8$ radiate only a few percent of their angular momentum until they reach a more strongly bound state. This explains the approximate

TABLE II. The transition times t_{32} (t_{21}) it takes a sequence 3 (2) model to radiate an amount of gravitational wave energy corresponding to the difference in binding energy from sequence 2 (1). The amount of angular momentum $\Delta J_{\rm rad}/M_{\rm ADM}^2$ for models near the critical orbital angular momentum $L_{\rm crit}$ radiated up to this time is small compared with the initial orbital angular momentum L/M^2 listed in Table I.

	seq3 → seq2			seq2 → seq1	
L/M^2	$T_{32}/M_{\rm ADM}$	$\Delta J_{\rm rad}/M_{\rm ADM}^2(t_{32})$	L/M^2	$t_{21}/M_{\rm ADM}$	$\Delta J_{\rm rad}/M_{\rm ADM}^2(t_{21})$
1.020	1646	0.145	0.873	91	0.020
1.021	1653	0.145	0.873	98	0.022
1.011	1450	0.130	0.868	106	0.023
0.984	926	0.112	0.839	106	0.021
0.931	444	0.082	0.765	108	0.017
0.841	203	0.055	0.612	114	0.014
0.704	201	0.042	0.350	127	0.010

universality of models belonging to different sequences, but having the same initial orbital angular momentum.

V. PERTURBATIVE ESTIMATES OF THE FINAL ANGULAR MOMENTUM OF ECCENTRIC BINARY BLACK-HOLE COALESCENCE

A simple, surprisingly successful model to compute the spin of the final black hole for binaries in quasicircular orbits has recently been proposed by Buonanno, Kidder and Lehner [57]. Here we discuss extensions of that model to eccentric binaries. The model introduced in Ref. [57] is based on three main assumptions: (i) the gravitational energy radiated after the formation of a common apparent horizon is a second order quantity, and has a small effect on the spin of the final hole; (ii) the magnitude of the individual spins remains constant during the inspiral, and (iii) most of the angular momentum is radiated during the long inspiral stage until the system reaches the innermost stable circular orbit (ISCO). A crucial final ingredient of the model is to estimate the contribution of the orbital angular momentum to the final spin by associating it with the orbital angular momentum of a point particle orbiting a Kerr black hole with spin parameter $j_{\rm fin}$ corresponding to the *final* hole.

The generalization of this model to eccentric orbits is straightforward, if one identifies the ISCO with the separatrix, or innermost stable bound orbit [83,84] (see the appendix for details). Following [57], in the general case of eccentric orbits we write the (approximate) conservation equation

$$j_{\rm fin} = \frac{L_{\rm sep}(j_{\rm fin}, e_p)}{M^2} + \frac{M_1 a_1}{M^2} + \frac{M_2 a_2}{M^2}, \qquad (5.1)$$

where a_i is the Kerr parameter of each hole, the eccentricity e_p for point-particle geodesics is defined in Eq. (A6) and $L_{\rm sep}(j_{\rm fin}, e_p)$ is the orbital angular momentum at the separatrix, computed within a point-particle framework. A prescription for the computation of this quantity is given in the appendix. Note that e_p is defined in terms of coordinate positions of the particle, and therefore there is no direct physical relation between e_p and the eccentricity quantifiers discussed above. Assuming without loss of generality that $M_1 \geq M_2$, we can rewrite Eq. (5.1) as

$$j_{\rm fin} = \frac{L_{\rm sep}(j_{\rm fin}, e_p)}{M^2} + \frac{j_1}{4}(1+\sqrt{1-4\eta})^2 + \frac{j_2}{4}(1-\sqrt{1-4\eta})^2, \qquad (5.2)$$

where $j_i = a_i/M_i$ and η, as usual, denotes the symmetric mass ratio.

We will focus on the special case where the initial spins have equal magnitude, $j_1 = j_2$. In Fig. 9 (left panel) we show the predicted spin of the final hole as a function of the symmetric mass ratio η when both initial spins are aligned with the orbital angular momentum. The effect of eccentricity is always mild, and for all values of the initial spin magnitude, eccentricity tends to *increase* the spin of the final hole.

Ref. [57] also predicted that, for circular orbits, the final spin of the remnant should increase as the mass ratio $q \to 1$ (i.e., as $\eta \to 1/4$) for $j_i \lesssim j_{\rm crit}$, while it should decrease as $q \to 1$ if $j_i \gtrsim j_{\rm crit}$. They estimated $j_{\rm crit} \simeq 0.948$. At the critical value, any merger will leave the final spin essentially unchanged, irrespective of the mass ratio q. This expectation is confirmed by our calculations (see the inset

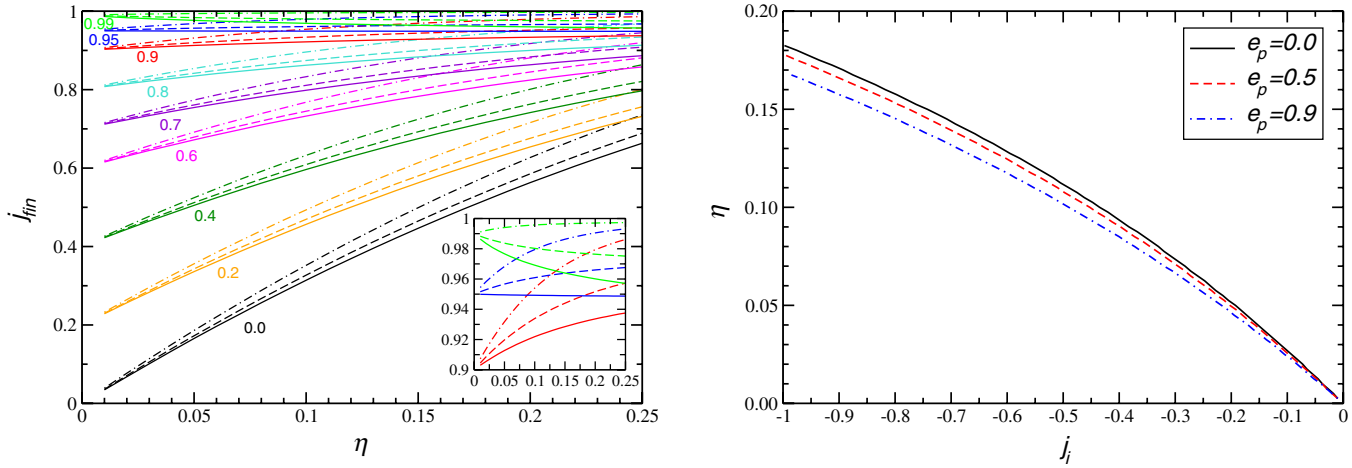

FIG. 9 (color online). Left panel: predicted angular momentum by point-particle extrapolation of results from perturbation theory. Solid, dashed and dash-dotted lines assume a point-particle eccentricity $e_p = 0$, 0.5 and 0.9, respectively (see appendix for a definition of this eccentricity parameter, not to be confused with the Newtonian eccentricity). Numbers next to each set of lines denote different values of $j_i = j_1 = j_2$, and the initial spin on each hole is assumed to be aligned with the orbital angular momentum. Right panel: we assume the initial spin on each hole to be antialigned with the orbital angular momentum ($j_i = j_1 = j_2 < 0$). For various eccentricities (as indicated in the legend) we show the functional dependence between mass ratio and j_i needed to produce a final nonspinning hole.

TABLE III. Estimated critical value of the Kerr parameter $j_{\rm crit}$ (see text) for selected values of the eccentricity e_p, as defined perturbatively (see appendix).

	$e_p = 0.0$	$e_p = 0.1$	$e_p = 0.2$	$e_p = 0.5$	$e_p = 0.9$
$j_i^{\rm crit}$	0.948	0.950	0.953	0.972	0.998

of the left panel of Fig. 9). However, since a nonzero eccentricity always tends to increase the final spin, $j_{\rm crit}$ grows with eccentricity.

Table III shows the critical value of the initial Kerr parameter $j_i^{\rm crit} = j_1 = j_2$ as a function of the eccentricity (as defined perturbatively). For large eccentricities $e_p \sim 1$ the critical Kerr parameter is very close to the maximum possible value, $j_i^{\rm crit} \sim 1$: in other words, for large eccentricities the final spin should always *increase* as we approach the equal-mass limit. Therefore we conjecture that the maximum spin $j_{\rm fin} \simeq 0.724$ that we found in our sequence of equal-mass merger simulations should be an *absolute upper limit* on the spin that can be achieved as the end-product of nonspinning black-hole mergers: unequal-mass mergers should always produce smaller final spins.

An interesting question explored in [57] concerns spin-flip configurations. Suppose that initially both black holes have equal Kerr parameters $j_i = j_1 = j_2$, and spins *anti-aligned* with respect to the orbital angular momentum. What is the value of the symmetric mass ratio η for which the inspiral produces a Schwarzschild black hole, as a function of j_i? As argued in [57] these critical configurations could be particularly interesting, since mild variations of the parameters around the critical values may produce interesting orbital dynamics (e.g. spin flips) and complex gravitational waveforms.

The critical curve predicted by the model has been shown to yield good agreement with numerical simulations, especially for spins aligned with the orbital angular momentum [85,86]. In particular, our study [86] obtains for a mass ratio $q = 4$ and initial dimensionless Kerr parameters of the individual holes $j_i = -0.75$, -0.8 and -0.85 a final Kerr parameter $j_{\rm fin} = 0.0533$, 0.0237 and -0.0038, respectively, thus bracketing the formation of a Schwarzschild hole. For comparison, for zero eccentricity Eq. (5.2) yields $j_i = -0.815\,083$, while the fitting formula in [85] yields $j_i = -0.823\,462$. Details of this study, together with a multipolar analysis of several spinning configurations, are given in Ref. [86]. As shown in the right panel of Fig. 9, the effect of eccentricity on the location of these spin-flip configurations is very mild. For a fixed mass ratio, we predict that the magnitude of the (antialigned) spins required to produce a Schwarzschild black hole as the result of the merger should increase with eccentricity.

Considering the remarkable success of point-particle extrapolations, some words of caution are required. First of all, when we extrapolate results to comparable masses we should not attach any special meaning to the actual values of the point-particle eccentricity, since we do not know how that notion translates into the different PN definitions discussed in Sec. II. At best, we can only expect that the PN eccentricities are related to the perturbative eccentricity, as implicitly defined in Eq. (A6), by some monotonically increasing functional dependence.

Furthermore, we should not forget that the model proposed in [57] is only an approximation: for example, for a merger of equal-mass, nonspinning holes the model predicts a Kerr parameter $j_{\rm fin} = 0.663$ for the final hole, to be compared with $j_{\rm fin} \simeq 0.691$ from our numerical simulations (see also [22]).

Despite these ambiguities and limitations, the point-particle model can still make remarkable predictions. For example, we can ask the following question: if we consider a nonspinning black-hole binary, how much can we increase the Kerr parameter of the final hole by setting the binary in an eccentric orbit? We showed in Fig. 9 that, according to point-particle extrapolations, the final Kerr parameter should increase monotonically with eccentricity. Despite the unclear meaning of the eccentricity parameter, it is reasonable to assume that the maximum increase in the final Kerr parameter for nonspinning binaries should be $\Delta j_{\rm fin}^{\rm max} = j_{\rm fin}(e_p = 1) - j_{\rm fin}(e_p = 0) \simeq 0.750 - 0.663 \simeq 0.087$. As the motion turns into a plunge, $j_{\rm fin}$ should again decrease. From the results listed in Table I we can read out the "true," general relativistic prediction for the maximal spin increase induced by orbital eccentricity: $\Delta j_{\rm fin}^{\rm max} = 0.724 - 0.691 \simeq 0.033$. The level of agreement with simple extrapolations from perturbation theory is, once again, really surprising.

Finally, it is interesting to ask if we can use the eccentricity-induced increase of the final Kerr parameter to violate the cosmic censorship conjecture, by producing a final object with $j_{\rm fin} > 1$. In principle this could be possible: even for zero eccentricity, if we consider maximally spinning black holes ($j_1 = j_2 = 1$) with spins aligned to the orbital angular momentum, according to the point-particle extrapolation the final spin resulting from an equal-mass merger is $j_{\rm fin} = 0.959$, which is very close to the Kerr bound [57]. In fact, extrapolation of point-particle results suggests that cosmic censorship will *not* be violated. From the previous discussion it should be clear that the most "dangerous" situation corresponds to maximal eccentricities ($e_p = 1$). In this case, the extrapolation of point-particle results can be performed analytically. The expression for general initial spins and general mass ratio is too cumbersome to display here. If we consider equal-mass binaries, we get

$$j_{\rm fin} = \frac{j_1 + j_2}{4} + \frac{3 + \sqrt{9 - 4(j_1 + j_2)}}{8}. \qquad (5.3)$$

From this equation we are led to conjecture that *Kerr black holes produced as the result of a merger always satisfy the*

Kerr bound. The bound is only saturated when $e_p = 1$ and $j_1 = j_2 = 1$.

If instead we drop the equal-mass assumption, but we consider $j_i = j_1 = j_2$ (and again $e_p = 1$), we get the following expression for the final spin:

$$j_{\rm fin} = j_i + 2\eta[(1 - j_i - \eta) + \sqrt{(1 - 2\eta)(1 - j_i) + \eta^2}]. \tag{5.4}$$

This suggests that in the $j_i \to 1$ limit, $j_{\rm fin} \to 1$ for *any* mass ratio.

Early numerical simulations of spinning black-hole binary coalescence support our conjecture: quasicircular black-hole binaries with spins aligned to the orbital angular momentum tend to radiate excess angular momentum by undergoing a longer inspiral, or "orbital hang-up," and they never seem to produce naked singularities [78,85,87,88]. It will be interesting to see if this conclusion holds true, as we predict, when the black-hole binary is both spinning *and* highly eccentric.

VI. THE RINGDOWN WAVEFORM

It is well known that frequencies and quality factors of ringdown waveforms encode information about the properties of the Kerr black hole produced as a result of the merger (see [89] and references therein). Here we use the matrix pencil method to estimate time variations in the frequencies and quality factors of the dominant multipole ($\ell = 2$, $m = 2$) as we reduce the orbital angular momentum of the orbit. This and other methods have been discussed at length in Refs. [22,90], and we will not repeat that discussion here. An introduction to Prony methods to estimate parameters of complex exponentials in noise, in the context of black-hole perturbation theory, can be found in Ref. [90]. To remove boundary reflection noise from our simulations, we use the procedure described in [22] for quasicircular inspiral simulations.

In Fig. 10 we show the time dependence of the estimated (dimensionless) QNM frequency $M\omega_R$ and of the quality factor Q for the dominant multipolar component ($\ell = m = 2$) of the radiation. All quantities are plotted as functions of the starting time for the fit t_0, as measured from the time $t_{\rm peak}$ corresponding to the maximum in the modulus of the waveform's amplitude $|\psi_{22}(t_{\rm peak})|$. We see the same features we observed in [22,90]. After a short transient for $t_0 - t_{\rm peak} \lesssim 10M$, frequencies and quality factors become roughly constant, except at very late times, where the ringdown signal is very small and noise contaminates the estimates. Frequency estimates are usually better than quality factor estimates, and temporal variations in both quantities (which are probably induced by noise in the simulations) become more significant for the shorter, plunging configurations with low values of P/M.

The quality factor is a dimensionless quantity, and as such it can only depend on the dimensionless Kerr parameter of the final hole: $Q = Q(j_{\rm fin})$. The Kerr parameter can then be obtained by inverting this relation. We perform the inversion by interpolating QNM tables [89]. Results are shown in Fig. 11. There we discard all points for which we get unphysical black-hole parameters (e.g. points for which the final estimated black-hole mass $M_{\rm fin} > M_{\rm ADM}$).

Unfortunately, estimates of the final angular momentum become less reliable as $L/M^2 \to 0$. The reason is apparent by looking, for example, at the right panel of Fig. 5 in Ref. [89]. As the spin of the final hole decreases, and, in particular, for $j_{\rm fin} \lesssim 0.5$, relatively large variations in the Kerr parameter produce mild variations in the $\ell = m = 2$ quality factor. Conversely, small oscillations in Q produce large variations in $j_{\rm fin}$. From Fig. 10 we see that noise-induced variations in Q actually *increase* for near head-on collisions. Therefore, QNM based estimates of the Kerr

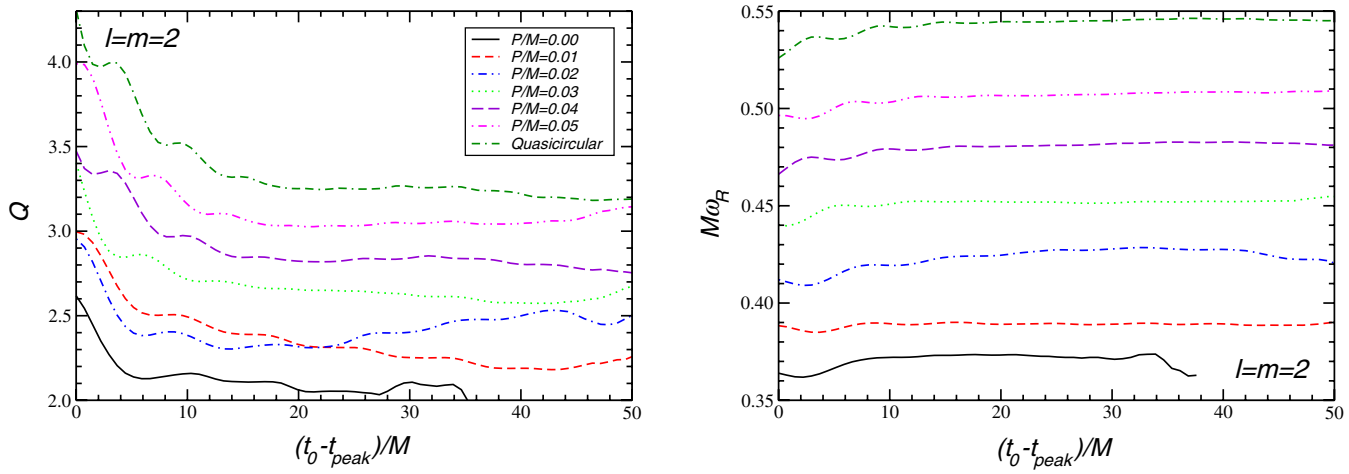

FIG. 10 (color online). Prony estimates for the quality factor Q (left) and dimensionless oscillation frequency $M\omega_R$ (right) of the fundamental mode with $\ell = m = 2$. Different line styles (see the legend in the left panel) refer to different models in sequence 1.

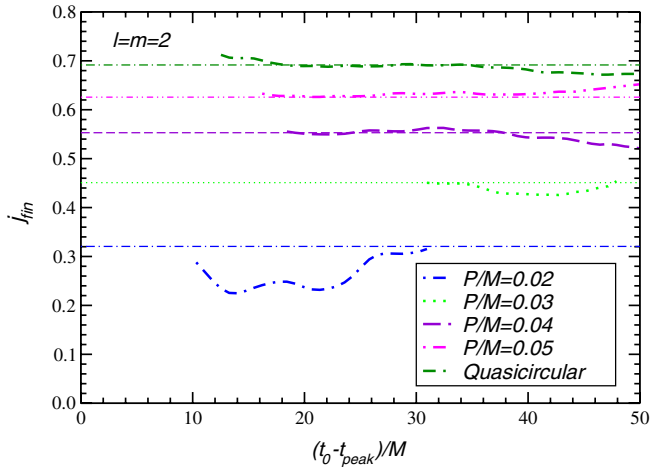

FIG. 11 (color online). Angular momentum estimate $j_{\rm fin}$ from Prony fits. Horizontal lines are estimates of the final Kerr parameter from energy balance arguments (see Table I).

parameter are sensibly affected by noise when $j_{\rm fin} \lesssim 0.5$. The situation becomes even worse when we consider higher multipoles. However, it is clear from Fig. 11 that QNM estimates are consistent (within the errors, which increase as $P/M \to 0$) with estimates obtained from angular momentum balance arguments.

Energy-maximized orthogonal projection

As discussed thoroughly in [22], there is no unique definition of the ringdown starting time, and correspondingly there is no unique way to define the fraction of energy radiated into ringdown for a given waveform. A useful measure of the ringdown energy is provided by the "energy-maximized orthogonal projection" (EMOP). In [22] the EMOP was shown to yield reasonable estimates of the ringdown radiation from nonspinning, unequal-mass black-hole binaries, and therefore we shall perform the same analysis on the present waveforms.

Our results are summarized in Table IV for sequence 1. Results for sequences 2 and 3 are very similar, and we do not show them here. Ref. [22] found that ringdown accounts for about 42% of the total energy emitted in the merger of nonspinning black-hole binaries in quasicircular orbits, i.e., $E_{\rm EMOP}/E_{\rm rad} \simeq 42\%$. In the second column of Table IV we show the corresponding results for the present simulations. As a general trend, higher eccentricity means that the black holes spend less time orbiting each other before merger. Therefore one expects that the relative ringdown content, as measured by $E_{\rm EMOP}/E_{\rm rad}$, should increase with eccentricity, since less energy is radiated during the premerger phase. This trend is clearly visible in Table IV. On the other hand, the ringdown starting time $\langle t_{\rm EMOP}\rangle$, as measured from $t_{\rm peak}$, is insensitive to the eccentricity of the run. This is consistent with the idea that ringdown is associated with the formation of a deformed common apparent horizon, and it should not depend on the details of the process leading to the formation of the horizon. Finally, in the last entry of Table IV we show the fraction of the total ADM mass radiated in ringdown waves. This number is important for estimates of ringdown detectability with both Earth-based GW detectors and LISA [89,91]. A polynomial fit as a function of the dimensionless orbital angular momentum yields

$$\frac{\langle E_{\rm EMOP}\rangle}{M_{\rm ADM}} = 10^{-2}\left[0.11\text{–}1.55\left(\frac{L}{M^2}\right) + 4.22\left(\frac{L}{M^2}\right)^2\right], \quad (6.1)$$

where (as in Table IV) angular brackets denote an average over the two polarizations.

TABLE IV. EMOP data for $l = 2$. Numbers separated by a comma correspond to the $+$ and $\times$ polarizations, respectively. The fraction of the total energy in ringdown is strongly dependent on the eccentricity. We find that, independently of the run, the value of $t_{\rm EMOP}$ for a given polarization is generally at a fixed position relative to the maximum of the waveform's amplitude $t_{\rm peak}$. We measure this relative difference by $\Delta t_{\rm EMOP} \equiv t_{\rm peak} - t_{\rm EMOP}$. Angular brackets denote an average over the two polarizations.

P/M	$\frac{E_{\rm EMOP}}{E_{\rm rad}}$	$\frac{\langle t_{\rm EMOP}\rangle}{M_{\rm ADM}}$	$\frac{\Delta t_{\rm EMOP}}{M_{\rm ADM}}$	$\frac{\langle \Delta t_{\rm EMOP}\rangle}{M_{\rm ADM}}$	$\frac{\langle 10^2 E_{\rm EMOP}\rangle}{M_{\rm ADM}}$
0.14	0.42, 0.41	230.5	9.1, 6.1	7.6	0.0164
0.1383	0.40, 0.41	312.2	4.9, 8.4	6.6	0.0149
0.13	0.43, 0.40	230.2	8.1, 4.6	6.3	0.0158
0.12	0.42, 0.43	222.2	5.2, 8.7	6.9	0.0181
0.11	0.44, 0.42	214.2	9.3, 5.8	7.6	0.0171
0.10	0.46, 0.45	198.2	10.0, 13.6	11.8	0.0222
0.09	0.48, 0.52	190.0	10.5, 7.5	9.0	0.0207
0.08	0.56, 0.58	183.8	6.1, 9.6	7.9	0.0183
0.07	0.61, 0.58	179.8	9.2, 5.7	7.4	0.0147
0.06	0.61, 0.65	177.0	5.0, 8.0	6.5	0.0111
0.05	0.68, 0.65	175.0	9.0, 5.0	7.0	0.007 75
0.04	0.69, 0.66	174.0	6.0, 10.0	8.0	0.004 83
0.03	0.66, 0.75	176.5	4.3, 8.3	6.3	0.002 34
0.02	0.72, 0.75	175.2	11.2, 6.8	9.0	0.001 31
0.01	0.73, 0.75	178.0	9.2, 6.2	7.7	0.000 617
0	0.77, $\cdots$	177.5	8.2, $\cdots$	8.2	0.000 475

VII. CONCLUSIONS AND OUTLOOK

We have presented a study of the gravitational waveforms produced by sequences of equal-mass, nonspinning black-hole binaries. For each sequence, the binding energy of the system is kept constant and the orbital angular momentum is progressively reduced to zero, producing orbits of increasing eccentricity and eventually a head-on collision. We find that the motion transitions from inspiral to plunge when the orbital angular momentum $L = L_{\rm crit} \simeq 0.8M$. For $L < L_{\rm crit}$ the binary always completes less than $\sim$1 orbit, and PN estimates of the orbital eccentricity are

no longer meaningful. As the initial momentum of the holes $P/M \to 0$ the polarization quickly becomes linear, rather than circular, and the radiated energy drops (roughly) exponentially. For equal-mass, nonspinning binaries, orbits with $L \simeq L_{\rm crit}$ produce the largest dimensionless Kerr parameter for the remnant, $j_{\rm fin} = J/M^2 \simeq 0.724 \pm 0.13$ (to be compared with the Kerr parameter $j_{\rm fin} \simeq 0.69$ resulting from quasicircular inspirals). These results are quite insensitive to the initial separation of the holes, and they can be understood using extrapolations from black-hole perturbation theory. Larger separations, as used in sequence 3, will be necessary to perform accurate comparisons with PN predictions for the evolution of eccentric binaries (see [51]). Such an analysis is beyond the scope of this work, however, and a corresponding analysis of the sequence 3 data will be presented elsewhere.

For equal masses, we found that eccentric binary mergers with $L \simeq L_{\rm crit}$ maximize the Kerr parameter of the final black hole. Using arguments based on point-particle extrapolations, we proposed two conjectures: (1) $j_{\rm fin} \simeq 0.724 \pm 0.13$ should be close to the largest Kerr parameter that can be produced by *any* nonspinning black-hole binary merger, independently of the binary's mass ratio; and (2) even if we consider maximally spinning holes with spins aligned with the orbital angular momentum, orbital eccentricity should *not* lead to violations of the cosmic censorship conjecture. It will be interesting to check these conjectures using numerical simulations of eccentric binaries with unequal masses and nonzero spins.

ACKNOWLEDGMENTS

We thank Clifford Will, Achamveedu Gopakumar, Christian Königsdörffer and Gerhard Schäfer for discussions about eccentricity in the PN formalism, and Luciano Rezzolla and Michele Vallisneri for comments on the manuscript. This work was supported in part by DFG Grant No. SFB/Transregio 7 "Gravitational Wave Astronomy." E. B.'s research was supported by a contract with NASA to the Jet Propulsion Laboratory, California Institute of Technology; by the National Science Foundation, under Grant No. PHY 03-53180; and by NASA, under Grant No. NNG06GI60 to Washington University. V. C.'s work was partially funded by Fundação para a Ciência e Tecnologia (FCT)–Portugal through Projects No. PTDC/FIS/64175/2006 and No. POCI/FP/81915/2007. We thank the DEISA Consortium (cofunded by the EU, FP6 Project No. 508830), for support within the DEISA Extreme Computing Initiative (www.deisa.org). Computations were performed at LRZ Munich and the Doppler and Kepler clusters at the Institute of Theoretical Physics of the University of Jena. We are grateful to the Center for Computational Physics (CFC) in Coimbra for granting us access to the Milipeia cluster.

APPENDIX: ORBITS OF POINT PARTICLES IN THE KERR GEOMETRY AND THE ANGULAR MOMENTUM AT THE SEPARATRIX

Here we consider a test body of mass m_p moving in a Kerr spacetime, and we neglect the radiation reaction (therefore we focus on purely geodesic motion). For simplicity, we only consider equatorial orbits. The equations of motion are given in Boyer-Lindquist coordinates by

$$r^2 \frac{dr}{d\tau} = \pm (V_r)^{1/2}, \tag{A1}$$

$$r^2 \frac{d\phi}{d\tau} = V_\phi \equiv -(M j_{\rm fin} \tilde{E} - \tilde{L}) + \frac{M j_{\rm fin} T}{\Delta}, \tag{A2}$$

$$r^2 \frac{dt}{d\tau} = V_{\rm t} \equiv -M j_{\rm fin}(M j_{\rm fin} \tilde{E} - \tilde{L}) + \frac{(r^2 + M^2 j_{\rm fin}^2) T}{\Delta}, \tag{A3}$$

$$\theta(\tau) = \pi/2, \tag{A4}$$

where $T = E(r^2 + M^2 j_{\rm fin}^2) - \tilde{L} M j_{\rm fin}$, $V_r = T^2 - \Delta(r^2 + (\tilde{L} - M j_{\rm fin}\tilde{E})^2)$, $\Delta = r^2 - 2Mr + M^2 j_{\rm fin}^2$. The two constants of motion

$$\tilde{E} \equiv E/m_p, \qquad \tilde{L} \equiv L/m_p, \tag{A5}$$

denote the orbit's specific energy and the z-component of angular momentum, respectively. We have prograde (retrograde) orbits according to whether $\tilde{L} > 0 (< 0)$. Bound orbits require $0 < \tilde{E} < 1$. A general bound equatorial orbit can equivalently be described either by the constants $\tilde{E}$ and $\tilde{L}$, or by a semilatus rectum p and an eccentricity e_p (with $0 \le e_p < 1$). The semilatus rectum measures the size of the orbit, and the eccentricity measures the degree of noncircularity. We define these parameters in terms of the two turning points of the orbit (r_p is the periastron and r_a the apastron):

$$r_p = \frac{p}{1 + e_p}, \qquad r_a = \frac{p}{1 - e_p}. \tag{A6}$$

The specific angular momentum and energy can be computed by solving the simultaneous equations for $\tilde{E}$ and $\tilde{L}$

$$\tilde{E} = \left[1 - \left(\frac{M}{p}\right)(1 - e_p^2)\left\{1 - \frac{x^2}{p^2}(1 - e_p^2)\right\}\right]^{1/2}, \tag{A7}$$

$$x^2 = \frac{-N(p, e_p) \mp \Delta_x^{1/2}(p, e_p)}{2F(p, e_p)}, \tag{A8}$$

where the upper (lower) sign corresponds to prograde (retrograde) motion, and we have defined

$$x = \tilde{L} - M j_{\rm fin} \tilde{E}. \tag{A9}$$

The explicit form of the functions F, N and Δ_x is

$$F(p, e_p) = \frac{1}{p^3}[p^3 - 2M(3 + e_p^2)p^2 + M^2(3 + e_p^2)^2 p - 4M^3 j_{\rm fin}^2(1 - e_p^2)^2], \quad \text{(A10)}$$

$$N(p, e_p) = \frac{2}{p}[-Mp^2 + M^2((3 + e_p^2) - j_{\rm fin}^2)p - M^3 j_{\rm fin}^2(1 + 3e_p^2)], \quad \text{(A11)}$$

$$\Delta_x(p, e_p) = N^2 - 4FM^2(j_{\rm fin}^2 - p/M)^2. \quad \text{(A12)}$$

In general there are three different radial turning points (i.e., roots of $V_r = 0$): the periastron at $r = r_p$, the apastron at $r = r_a$ and a third root $r = r_3$, defining a forbidden region. The case with $r_p = r_3$ corresponds to a marginally stable orbit: once at the periastron, the particle will enter into a circular orbit of radius r_p. This location has been called the innermost stable bound orbit [84], and it is the generalization of the ISCO for general eccentric orbits. At this stage the orbit has become unstable, so that a slight inwards "push" will drive the particle to plunge into the black hole. Therefore, stable bound orbits should satisfy $r_3 < r_p$. This translates to the inequality

$$x^2(1 + e_p)(3 - e_p) < p^2. \quad \text{(A13)}$$

The boundary curve defined by

$$p_s^2 = x^2(1 + e_p)(3 - e_p) \quad \text{(A14)}$$

defines the separatrix of bound orbits.

Equations (A7)–(A14) allow one to compute the energy and orbital angular momentum at the separatrix. Strictly speaking, these equations are only valid for point particles. The substitution

$$\tilde{L} \to \frac{L}{\eta M} \quad \text{(A15)}$$

should provide a reasonable extrapolation to the general finite mass-ratio case.

[1] A. Abramovici *et al.* (LIGO Collaboration), Science **256**, 325 (1992).
[2] H. Lück, Classical Quantum Gravity **14**, 1471 (1997).
[3] M. Ando *et al.*, Phys. Rev. Lett. **86**, 3950 (2001).
[4] B. Caron *et al.*, Classical Quantum Gravity **14**, 1461 (1997).
[5] K. Danzmann *et al.*, "LISA: Pre-Phase A Report," 2nd ed., 1998.
[6] F. Pretorius, Phys. Rev. Lett. **95**, 121101 (2005).
[7] M. Campanelli, C. O. Lousto, P. Marronetti, and Y. Zlochower, Phys. Rev. Lett. **96**, 111101 (2006).
[8] J. G. Baker, J. Centrella, D.-I. Choi, M. Koppitz, and J. van Meter, Phys. Rev. Lett. **96**, 111102 (2006).
[9] F. Pretorius, Classical Quantum Gravity **23**, S529 (2006).
[10] J. G. Baker, J. Centrella, D.-I. Choi, M. Koppitz, and J. van Meter, Phys. Rev. D **73**, 104002 (2006).
[11] M. Campanelli, C. O. Lousto, and Y. Zlochower, Phys. Rev. D **73**, 061501(R) (2006).
[12] U. Sperhake, Phys. Rev. D **76**, 104015 (2007).
[13] M. A. Scheel, H. P. Pfeiffer, L. Lindblom, L. E. Kidder, O. Rinne, and S. A. Teukolsky, Phys. Rev. D **74**, 104006 (2006).
[14] B. Brügmann, M. González, M. Hannam, S. Husa, U. Sperhake, and W. Tichy, Phys. Rev. D **77**, 024027 (2008).
[15] F. Herrmann, I. Hinder, D. Shoemaker, P. Laguna, and R. Matzner, arXiv:gr-qc/0701143.
[16] D. Pollney *et al.*, Phys. Rev. D **76**, 124002 (2007).
[17] Z. B. Etienne, J. A. Faber, Y. T. Liu, S. L. Shapiro, and T. Baumgarte, Phys. Rev. D **76**, 101503 (2007).
[18] J. G. Baker, J. R. van Meter, S. T. McWilliams, J. Centrella, and B. J. Kelly, Phys. Rev. Lett. **99**, 181101 (2007).
[19] J. D. Schnittman and A. Buonanno, arXiv:astro-ph/0702641.
[20] M. Hannam, S. Husa, J. A. González, U. Sperhake, and B. Brügmann, Phys. Rev. D **77**, 044020 (2008).
[21] A. Buonanno, G. B. Cook, and F. Pretorius, Phys. Rev. D **75**, 124018 (2007).
[22] E. Berti *et al.* Phys. Rev. D **76**, 064034 (2007).
[23] M. Boyle, D. A. Brown, L. E. Kidder, A. H. Mroue, H. P. Pfeiffer, M. A. Scheel, G. B. Cook, and S. A. Teukolsky, Phys. Rev. D **76**, 124038 (2007).
[24] J. D. Schnittman *et al.*, Phys. Rev. D **77**, 044031 (2008).
[25] P. Ajith *et al.*, Classical Quantum Gravity **24**, S689 (2007).
[26] Y. Pan, A. Buonanno, J. G. Baker, J. Centrella, B. J. Kelly, S. T. McWilliams, F. Pretorius, and J. R. van Meter, Phys. Rev. D **77**, 024014 (2008).
[27] B. Vaishnav, I. Hinder, F. Herrmann, and D. Shoemaker, Phys. Rev. D **76**, 084020 (2007).
[28] P. Ajith *et al.*, Phys. Rev. D **77**, 104017 (2008).
[29] M. Campanelli, C. O. Lousto, and Y. Zlochower, Phys. Rev. D **77**, 101501 (2008).
[30] P. C. Peters and J. Mathews, Phys. Rev. **131**, 435 (1963).
[31] L. Wen, Astrophys. J. **598**, 419 (2003).
[32] M. Dotti, M. Colpi, and F. Haardt, Mon. Not. R. Astron. Soc. **367**, 103 (2006).
[33] M. Dotti, M. Colpi, F. Haardt, and L. Mayer, Mon. Not. R. Astron. Soc. **379**, 956 (2007).
[34] L. Mayer *et al.*, Science **316**, 1874 (2007).
[35] G. D. Quinlan, New Astron. Rev. **1**, 35 (1996).
[36] S. J. Aarseth, Astrophys. Space Sci. **285**, 367 (2003).
[37] P. Berczik, D. Merritt, and R. Spurzem, Astrophys. J. **633**, 680 (2005).
[38] P. Berczik, D. Merritt, R. Spurzem, and H.-P. Bischof, Astrophys. J. **642**, L21 (2006).

[39] T. Matsubayashi, J. Makino, and T. Ebisuzaki, Astrophys. J. **656**, 879 (2007).
[40] P. J. Armitage and P. Natarajan, Astrophys. J. **634**, 921 (2005).
[41] C. F. Sopuerta, N. Yunes, and P. Laguna, Astrophys. J. **656**, L9 (2007).
[42] L. E. Kidder, C. M. Will, and A. G. Wiseman, Phys. Rev. D **47**, 3281 (1993).
[43] A. Buonanno and T. Damour, Phys. Rev. D **62**, 064015 (2000).
[44] A. Ori and K. S. Thorne, Phys. Rev. D **62**, 124022 (2000).
[45] A. Buonanno, Y. Chen, and T. Damour, Phys. Rev. D **74**, 104005 (2006).
[46] E. Berti and V. Cardoso, Phys. Rev. D **74**, 104020 (2006).
[47] A. Buonanno *et al.*, Phys. Rev. D **76**, 104049 (2007).
[48] F. Pretorius and D. Khurana, Classical Quantum Gravity **24**, S83 (2007).
[49] M. C. Washik, J. Healy, F. Herrmann, I. Hinder, D. Shoemaker, P. Laguna, and R. A. Matzner, Phys. Rev. Lett. **101**, 061102 (2008).
[50] I. Hinder, B. Vaishnav, F. Herrmann, D. Shoemaker, and P. Laguna, Phys. Rev. D **77**, 081502 (2008).
[51] I. Hinder, F. Herrmann, P. Laguna, and D. Shoemaker, arXiv:0806.1037.
[52] S. B. Giddings, AIP Conf. Proc. **957**, 69 (2007).
[53] T. Dray and G. 't Hooft, Nucl. Phys. **B253**, 173 (1985).
[54] S. B. Giddings, D. J. Gross, and A. Maharana, Phys. Rev. D **77**, 046001 (2008).
[55] V. Cardoso, E. Berti, and M. Cavaglia, Classical Quantum Gravity **22**, L61 (2005).
[56] U. Sperhake, V. Cardoso, F. Pretorius, E. Berti, and J. A. Gonzalez, arXiv:0806.1738.
[57] A. Buonanno, L. E. Kidder, and L. Lehner, Phys. Rev. D **77**, 026004 (2008).
[58] R.-M. Memmesheimer, A. Gopakumar, and G. Schäfer, Phys. Rev. D **70**, 104011 (2004).
[59] T. Damour and N. Deruelle, Ann. Inst. Henri Poincaré, A **43**, 107 (1985).
[60] T. Mora and C. M. Will, Phys. Rev. D **69**, 104021 (2004).
[61] T. Damour and G. Schafer, Nuovo Cimento Soc. Ital. Fis. B **101**, 127 (1988).
[62] G. Schafer and N. Wex, Phys. Lett. A **174**, 196 (1993); 461 (E) (1993).
[63] M. Tessmer and A. Gopakumar, Mon. Not. R. Astron. Soc. **374**, 721 (2007).
[64] E. Berti, S. Iyer, and C. M. Will, Phys. Rev. D **74**, 061503 (2006).
[65] J. D. Grigsby and G. B. Cook, Phys. Rev. D **77**, 044011 (2008).
[66] S. Husa, J. A. González, M. D. Hannam, B. Brügmann, and U. Sperhake, Phys. Rev. D **77**, 044037 (2008).
[67] H. P. Pfeiffer *et al.*, Classical Quantum Gravity **24**, S59 (2007).
[68] J. G. Baker *et al.*, Phys. Rev. D **75**, 124024 (2007).
[69] Cactus Computational Toolkit homepage: http://www.cactuscode.org/.
[70] S. Brandt and B. Brügmann, Phys. Rev. Lett. **78**, 3606 (1997).
[71] S. Husa, J. A. Gonzalez, M. Hannam, B. Brügmann, and U. Sperhake, Classical Quantum Gravity **25**, 105006 (2008).
[72] E. Schnetter, S. H. Hawley, and I. Hawke, Classical Quantum Gravity **21**, 1465 (2004).
[73] Carpet Code homepage: http://www.carpetcode.org/.
[74] J. Thornburg, Phys. Rev. D **54**, 4899 (1996).
[75] J. Thornburg, Classical Quantum Gravity **21**, 743 (2004).
[76] M. Ansorg, B. Brügmann, and W. Tichy, Phys. Rev. D **70**, 064011 (2004).
[77] J. M. Bowen and J. W. York, Jr., Phys. Rev. D **21**, 2047 (1980).
[78] P. Marronetti, W. Tichy, B. Brugmann, J. A. Gonzalez, and U. Sperhake, Phys. Rev. D **77**, 064010 (2008).
[79] L. E. Kidder, Phys. Rev. D **77**, 044016 (2008).
[80] U. Sperhake, B. J. Kelly, P. Laguna, K. L. Smith, and E. Schnetter, Phys. Rev. D **71**, 124042 (2005).
[81] U. Sperhake, B. Brügmann, Jose A. González, M. D. Hannam, and S. Husa, arXiv:0705.2035.
[82] L. Gualtieri, E. Berti, V. Cardoso, and U. Sperhake, Phys. Rev. D **78**, 044024 (2008).
[83] C. Cutler, D. Kennefick, and E. Poisson, Phys. Rev. D **50**, 3816 (1994).
[84] K. Glampedakis and D. Kennefick, Phys. Rev. D **66**, 044002 (2002).
[85] L. Rezzolla *et al.*, Astrophys. J. **674**, L29 (2008).
[86] E. Berti, V. Cardoso, J. A. Gonzalez, U. Sperhake, and B. Brugmann, Classical Quantum Gravity **25**, 114035 (2008).
[87] M. Campanelli, C. O. Lousto, and Y. Zlochower, Phys. Rev. D **74**, 041501 (2006).
[88] L. Rezzolla *et al.*, Astrophys. J. **679**, 1422 (2008).
[89] E. Berti, V. Cardoso, and C. M. Will, Phys. Rev. D **73**, 064030 (2006).
[90] E. Berti, V. Cardoso, J. A. Gonzalez, and Ulrich Sperhake, Phys. Rev. D **75**, 124017 (2007).
[91] E. Berti, J. Cardoso, V. Cardoso, and M. Cavaglia, Phys. Rev. D **76**, 104044 (2007).